國立臺灣大學理學院物理學研究所
碩士論文

Department of Physics
College of Science
National Taiwan University
Master Thesis

帶有隨機雜訊的隨機標竿分析法
Randomized Benchmarking in the Presence of Stochastic
Noise

姜喆
Che Chiang

指導教授：管希聖 博士
Advisor: Hsi-Sheng Goan, Ph.D.

中華民國 111 年 7 月
July 18, 2022

Acknowledgements

I would like to express my deepest thanks to my advisor Hsi-Sheng Goan for his help. I also thank my colleagues Chia-Hsien Huang, I-Chun Hsu, and Yun Chih Liao for their useful suggestions and help with thesis writing.

摘要

　　以量子閘為基礎的量子計算，計算過程包含量子態初始化、量子閘運算以及量測運算結果三個階段。隨機標竿分析法提供一套檢驗流程僅評估量子閘運算階段的誤差，排除掉量子態初始化及量測運算結果的影響。不過，隨機標竿分析法的理論推導假設了不同量子閘的雜訊都相同且不會隨時間變化，若系統包含其他類型雜訊，隨機標竿分析法是否仍然適用需要進一步的理論分析。目前已經有理論考慮了不會隨時間變化但每個量子閘雜訊不同的隨機標竿分析法。本論文將建立在這個新的理論基礎上，把隨機標竿分析法的適用範圍推廣到隨時間隨機變化的雜訊，並將推廣後的隨機標竿分析法量測結果與閘平均保真度做比較。我們進行了單量子位元與雙量子位元的模擬來驗證理論，所有模擬都使用帶有去相位雜訊的哈密頓算符建構出帶有雜訊的量子閘，以此來進行隨機標竿分析法。

　　關鍵字：基於閘的量子電腦、隨機標竿分析法、隨機雜訊、量子閘運算、閘平均保真度
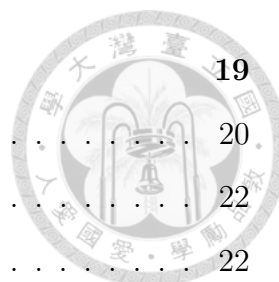
Abstract

Randomized benchmarking (RB) provides a procedure for estimating the average gate fidelity excluding state-preparation and measurement (SPAM) errors. However, the rigorous analyses of the standard RB protocol assume that noise should be gate-independent and time-independent. Later, the assumption was relaxed to gate-dependent and time-independent noise, while the decay parameter given in the RB fitting formula is no longer yielding the average gate fidelity. In this thesis, we consider RB under different types of stochastic noise. We provide a formula to fit the non-exponential decay fidelity obtained from RB with the explanation of the fitting result. We perform numerical simulations to verify our theories. The simulations consider the gate-dependent noise induced from the Hamiltonian with dephasing interference, and is executed on a typical single-qubit Hamiltonian, and a two-qubit Hamiltonian based on the experimental parameters from a real silicon-based quantum-dot device.

Keywords: Gate-based quantum computer, Randomized benchmarking, Stochastic noise, Quantum gate operations, Average gate fidelity

Contents

List of Figures

List of Tables

Chapter 1

Introduction

Quantum computers promise speedup over classical algorithms in specific problems such as factoring large semi-primes with exponential speedup [3] and searching an unstructured database with quadratic speedup [4]. Universal quantum operations not only requires scalable qubit technology but also need quantum error correction protocols that demand a sufficiently small error rate during the whole process including qubit state initialization, gate operation, and readout. The randomized benchmarking (RB) protocol provides a method to pick up errors resulting from only gate operation stage regardless of state preparation and measurement (SPAM) errors, which can help quantum computing experimentalists figure out the error sources.

However, the rigorous analyses of the standard RB protocol make an assumption that noise should be gate-independent and time-independent [5]. The simple form of the fidelity decay under the assumption may introduce inaccuracies under complex noise models. Currently, there has been much research about what standard RB measures under different noise models [6–11]. Besides, some RB variants are developed to deal with specific types of noise [12–15]. Among all of these noise models, non-Markovian or highly time-correlated noise is widely seen in silicon-based quantum-dot quantum computing experiments with dominant low-frequency intensities in the noise spectrum [16–20]. Much research has proposed modified RB fitting formulae to fit the non-exponential fidelity decay resulting from this type of

noise [21–24]. However, the physical interpretation of the fitting parameters is still ambiguous.

In this thesis, we generalize the gate-dependent RB theories developed by Wallman in Ref. [11] to the stochastic noise channels. We propose probability density function RB (PDF RB) formula to fit the non-exponential fidelity decay caused by slow-changing noise. We provide a clear physical interpretation of the fitting parameters. We numerically simulate the randomized benchmarking under unitary noise induced from the imperfect Hamiltonian with dephasing fluctuation, comparing simulations with theoretical predictions to verify our stochastic noise RB analyses.

The remainder of this thesis is organized as follows. Chapter 2 introduces the notations and the background knowledge about the RB protocol. In Chapter 3, we review the original RB analyses in Ref. [5] and gate-dependent RB analyses in Ref. [11]. After that, we extend these analyses to stochastic noise RB. Chapter 4 introduces the single-qubit and two-qubit simulation models. Chapter 5 presents our results, including the RB simulation results with different types of noise and the discussions. We summarize in Chapter 6.

Chapter 2

Preliminaries

2.1 Notation

We use the following notation throughout this thesis. Some of the notations are

- All operators (also known as gates) applying to the quantum states (expressed in density operators) are denoted by Roman font (e.g., A). The n-qubit identity operator is I_n ($n = 1$ if there is no subscript).

- Ideal quantum channels are denoted by calligraphic font (e.g. $\mathcal{E}$). The ideal unitary channel $\mathcal{U}$ corresponding to a unitary operator U is $U(\rho) = U\rho U^\dagger$. The identity channel is denoted $\mathcal{I}$. We sometimes refer to a unitary channel as an operator (or a gate) to emphasize the correspondence of a unitary channel to a quantum operation.

- A noisy implementation of an ideal channel is denoted with an overset ˜ (e.g., $\tilde{\mathcal{E}}$ denotes the noisy implementation of $\mathcal{E}$).

- Channel composition is denoted by $\circ$ (e.g., $\mathcal{E}_2 \circ \mathcal{E}_1(\rho) = \mathcal{E}_2[\mathcal{E}_1(\rho)]$).

- The n-qubit depolarizing channel with depolarizing parameter p is defined as

$$\mathcal{D}_p(\rho) = p\rho + \frac{1-p}{2^n}I_n.$$

3

- Groups and sets will be denoted by boldface font (e.g., $\mathbf{G}$). The unitary group of degree d is denoted by $\mathbf{U}(d)$. The n-qubit Pauli group $\mathbf{P}_n$ is defined as

$$\mathbf{P}_n = \{\pm 1, \pm i\} \times \{I, X, Y, Z\}^{\otimes n},$$

where

$$I \equiv \sigma_0 = \begin{pmatrix} 1 & 0 \\ 0 & 1 \end{pmatrix}, \ X \equiv \sigma_1 = \begin{pmatrix} 0 & 1 \\ 1 & 0 \end{pmatrix},$$

$$Y \equiv \sigma_2 = \begin{pmatrix} 0 & -i \\ i & 0 \end{pmatrix}, \ Z \equiv \sigma_3 = \begin{pmatrix} 1 & 0 \\ 0 & -1 \end{pmatrix}.$$

The n-qubit Clifford group is defined as

$$\mathbf{C}_n = \{C \in \mathbf{U}(2^n) | P \in \mathbf{P}_n \to CPC^\dagger \in \mathbf{P}_n\}/\mathbf{U}(1).$$

- The set of the Pauli operators including the indentity is $\mathbf{P}_1^* = \{I, X, Y, Z\}$. This definition can be generalized to n-qubit Pauli basis $\mathbf{P}_n^* = \mathbf{P}_1^{*\otimes n}$.

- The cardinality of a set $\mathbf{G}$ is denoted by $|\mathbf{G}|$.

- The uniform average of a function f over a set $\mathbf{S}$ is denoted by

$$\mathbb{E}_{s\in\mathbf{S}}[f(s)] = \frac{1}{|\mathbf{S}|} \sum_{s\in\mathbf{S}} f(s).$$

- We use the Pauli transfer matrix (PTM) representation of quantum channels [25] (also known as the Liouville representation) wherever a concrete representation is required. The PTM representation of an n-qubit quantum channel $\mathcal{E}$, denoted $[\mathcal{E}]_{\mathrm{PTM}}$, is a $4^n \times 4^n$ matrix with the entry on the i-th row and the j-th column given by

$$[\mathcal{E}]_{\mathrm{PTM}}(i, j) = \mathrm{Tr}[P_i \mathcal{E}(P_j)],$$

4

where $\mathbf{P}_n^* = \{P_0, P_1, ..., P_{4^n-1}\}$.

- We will assume the reader is familiar with the concepts of Hamiltonian and Schrödinger equation in quantum mechanics. Sometimes we will use the traditional bra-ket notation (also known as the Dirac notation) for quantum states.

2.2 Unitary 2-Designs

First, consider spherical designs to gain more intuition for understanding unitary 2-designs.

A spherical design is a set of the points on the sphere that can approximate the infinite points on it "to some degree". For example, consider the average surface temperature of the Earth. If the surface temperature is constant everywhere, we can randomly choose one point to represent the average surface temperature of the Earth. This trivial case implies that any single point is a spherical 0-design, where the number "0" stands for real homogeneous polynomial functions of degree zero (constant surface temperature in this case).

If we want to approximate homogeneous functions with higher degree on the sphere, we need more uniformly distributed points to construct the design. In fact, for a 3-dimensional unit sphere, a tetrahedron is a spherical 2-design, a cube is a 3-design, and a dodecahedron is a 5-design [26]. We can define spherical designs on the d-dimensional unit sphere $\mathbf{S}(\mathbb{R}^d)$ formally as follows [27, 28].

Definition 2.1 *Let $p_t : \mathbf{S}(\mathbb{R}^d) \to \mathbb{R}$ be a polynomial function of homogeneous degree at most t defined on $\mathbf{S}(\mathbb{R}^d)$. A set $\mathbf{X} = \{x : x \in \mathbf{S}(\mathbb{R}^d)\}$ is a* **spherical t-design** *if*

$$\mathbb{E}_{x \in \mathbf{X}}[p_t(x)] = \int_{\mathbf{S}(\mathbb{R}^d)} p_t(u)d\mu(u), \qquad (2.1)$$

where μ is the normalized spherical measure. Thus $d\mu$ can be intuitively understood as a properly chosen infinitesimal volume that makes the integration uniform over $\mathbf{S}(\mathbb{R}^d)$. We will not go through the details about the measure theory in this thesis.

Unitary designs are analogous to spherical designs. The polynomials we defined for spherical designs are on the points in $\mathbf{S}(\mathbb{R}^d)$. For unitary t-designs, the polynomials are defined on the elements of matrices in $\mathbf{U}(d)$. Furthermore, we consider the polynomials with homogeneous degree (t, t) for unitary t-designs, meaning that they have homogeneous degree at most t for both matrix variable $U \in \mathbf{U}(d)$ and its complex conjugate U^*. For example, $f(U) = \text{Tr}(UU^*)/d$ is a homogeneous function with degree $(1, 1)$ since taking trace and division by a constant are linear functions. The formal definition for unitary t-design is as follows [27, 28].

Definition 2.2 *Let $P_{(t,t)}$ be a polynomial function of homogeneous degree at most t both in the entries of $U \in \mathbf{U}(d)$ and in the entries of U^*. A set of unitary matrices $\mathbf{V} = \{U : U \in \mathbf{U}(d)\}$ is a **unitary t-design** if*

$$\mathbb{E}_{U \in \mathbf{V}}[P_{(t,t)}(U)] = \int_{\mathbf{U}(d)} P_{(t,t)}(U) d\eta(U), \qquad (2.2)$$

where η is the normalized Haar measure in $\mathbf{U}(d)$. Once again, $d\eta$ can be interpreted as a properly chosen infinitesimal weighting function that makes the integration uniform over $\mathbf{U}(d)$ [29].

2.3 Twirling Quantum Channels

Let $\mathcal{E}$ be a quantum channel. Suppose $\mathcal{E}$ is conjugated by a unitary channel. This action modifies the channel $\mathcal{E}$ to

$$\mathcal{E} \mapsto \mathcal{U}^\dagger \circ \mathcal{E} \circ \mathcal{U}, \qquad (2.3)$$

where

$$\mathcal{U}(\rho) = U\rho U^\dagger$$
$$\mathcal{U}^\dagger(\rho) = U^\dagger \rho U$$

with $U \in \mathbf{U}(d)$. Intuitively, *twirling* a quantum channel with respect to a set $\mathbf{S}$ means taking the average of conjugations given in Eq. (2.3) with all the elements in $\mathbf{S}$ [27, 28, 30]. The set $\mathbf{S}$ can either be finite or infinite.
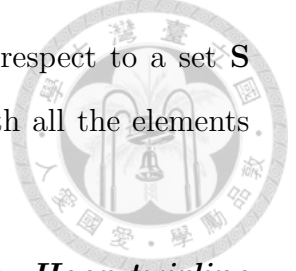
Definition 2.3 *Let η be the normalized Haar measure in $\mathbf{U}(2^n)$.* **Haar twirling** *maps an n-qubit quantum channel $\mathcal{E}$ to*

$$\mathcal{W}_H(\mathcal{E})(\rho) = \int_{\mathbf{U}(2^n)} d\eta(U) \, U^\dagger \mathcal{E}(U\rho U^\dagger) U. \tag{2.4}$$

Definition 2.4 **Clifford twirling** *maps an n-qubit quantum channel $\mathcal{E}$ to*

$$\mathcal{W}_C(\mathcal{E})(\rho) = \mathbb{E}_{C \in \mathbf{C}_n} \, C^\dagger \mathcal{E}(C\rho C^\dagger) C. \tag{2.5}$$

Haar twirling is equivalent to taking the average of conjugations with respect to all unitary operators. Since $U^\dagger \mathcal{E}(U\rho U^\dagger)U$ is a homogeneous polynomial with degree $(2, 2)$ and the Clifford group $\mathbf{C}_n$ is a unitary 2-design [27, 28], we can replace the integral in Eq. (2.4) with the discrete Clifford twirling. Thus for any channel $\mathcal{E}$, we have

$$\mathcal{W}_C(\mathcal{E})(\rho) = \mathcal{W}_H(\mathcal{E})(\rho). \tag{2.6}$$

2.4 Average Gate Fidelity

In quantum information theory, *fidelity* is a measure of the distance of two quantum states. The fidelity of two density operators ρ_1 and ρ_2 is defined to be [31]

$$\mathcal{F}(\rho_1, \rho_2) \equiv \left(\mathrm{Tr} \sqrt{\sqrt{\rho_1}\rho_2\sqrt{\rho_1}} \right)^2. \tag{2.7}$$

Consider a unitary channel $\mathcal{U}(\rho) = U\rho U^\dagger$. Define its noisy implementation to be $\tilde{\mathcal{U}} = \mathcal{U} \circ \Lambda$. Then restrict the input state to a pure state $\rho_\psi = |\psi\rangle \langle \psi|$. We define the state-dependent gate fidelity of the gate U as [5]

$$F_{\tilde{\mathcal{U}}, \mathcal{U}}(\psi) = F_{\Lambda, \mathcal{I}}(\psi) = \mathcal{F}(\rho_\psi, \Lambda(\rho_\psi)) = \mathrm{Tr}\left[\rho_\psi \Lambda(\rho_\psi)\right]. \tag{2.8}$$
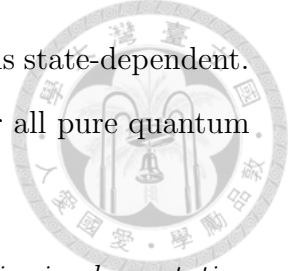
Equation (2.8) is not ideal for measuring the gate fidelity since it is state-dependent. Thus we obtain the *average gate fidelity* by integrating $F_{\tilde{\mathcal{U}},\mathcal{U}}$ over all pure quantum states.

Definition 2.5 *Let* $\mathcal{U}(\rho) = U\rho U^\dagger$ *be a unitary channel and its noisy implementation is defined to be* $\tilde{\mathcal{U}} = \mathcal{U} \circ \Lambda$. *The **average gate fidelity** of U is defined as*

$$F_{ave}(\tilde{\mathcal{U}}, \mathcal{U}) = F_{ave}(\Lambda, \mathcal{I}) = \int d\psi \, \mathrm{Tr}\left[\rho_\psi \Lambda(\rho_\psi)\right]. \tag{2.9}$$

Average gate fidelity of a depolarizing channel plays an important role in randomized benchmarking theory. If the noise can be expressed as a depolarizing channel $\mathcal{D}_p$, Eq. (2.9) is reduced to

$$F_{\mathrm{ave}}(\mathcal{D}_p, \mathcal{I}) = p + \frac{(1-p)}{2^n}. \tag{2.10}$$

In this thesis, we calculate the theoretical average gate fidelity using the function in IBM Qiskit package for Python [32]. The function in Qiskit uses a simpler formula with the input being the vectorized representation of the target quantum channel instead of carrying out the integral in Eq. (2.9). See [32–34].

The randomized benchmarking theories discussed in this thesis are related to noise channels being completely postivie and trace-preserving maps (CPTP). A central lemma used for the standard RB theory is as follows [5].

Lemma 1 *Haar twirling of a CPTP channel Λ produces the unique depolarizing channel $\mathcal{D}_p$ such that*

$$F_{ave}(\Lambda, \mathcal{I}) = F_{ave}(\mathcal{D}_p, \mathcal{I}). \tag{2.11}$$

We provide a brief explanation of Lemma 1 in Appendix A. The rigorous proof of Lemma 1 is given in Ref. [34].

Chapter 3

Randomized Benchmarking

This chapter is based mainly on [5] and [11], however we expand upon many of the results. We begin by introducing the randomized benchmarking protocol proposed in [5]. We show that RB makes several assumptions that the noise is Markovian and time- and gate-independent in order to properly estimate the average gate fidelity. We then discuss the analyses in [11] about what RB actually measures with Markovian and gate-dependent noise. The types of noise discussed in Ref. [5, 11] are constant in the sense that the noise strengths are fixed for the same quantum gates during the RB procedure. Finally, we consider RB with stochastic noise, which means that the noise strengths for the same quantum gates are randomly sampled from a specific probability density function.

The RB protocol for Clifford groups $\mathbf{C}_n$ is as follows [5].

1. Pick a Clifford gate length m.

2. Generate k sequences consisting of $(m + 1)$ quantum operations. The first m operations are randomly chosen from $\mathbf{C}_n$ and the $(m + 1)$-th operation is uniquely determined as the inverse of the composition of the first m gates.

3. Preparing the initial state ρ_ψ. For the ideal state preparation, $\rho_\psi = |\psi\rangle \langle\psi|$.

4. Operate each sequences from step 2 on the initial state ρ_ψ to get the final
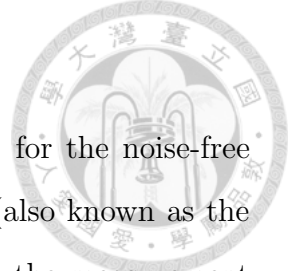
states ρ'_ψ.

5. Apply the POVM measurements E_ψ on ρ'_ψ ($E_\psi = |\psi\rangle\langle\psi|$ for the noise-free measurements). Measure the projection state probability (also known as the survival probability) $P(m) = \text{Tr}(E_\psi \rho'_\psi)$ by averaging over the measurement results from the k sequences.

6. Repeat steps 1-5 for different m to get the dataset $[m, P(m)]$. Then fit the results with the following decay model

$$P(m) = Ap^m + B \tag{3.1}$$

to estimate p.

A and B in Eq. (3.1) absorb the SPAM errors in the sense that they are independent of the gate length [5]. Thus the decay behavior of the projection state probability with increasing gate length is characterized by p. This implies that RB is robust to the SPAM errors.

Let $\tilde{\mathcal{C}}$ be an experimental implementation of an ideal Clifford channel $\mathcal{C}(\rho) = C\rho C^\dagger$. Assume that the decomposition of the i-th noisy Clifford gate $\tilde{\mathcal{C}}_i$ is $\tilde{\mathcal{C}}_i = \Lambda_{i,\delta} \circ \mathcal{C}_i$, where Λ is a CPTP map and δ is the noise strength parameter of the noise channel Λ. We refer to the noise channels as being "gate-independent" if the noise channels are independent of the Clifford gates thus the Clifford indices i for Λ are omitted. Similarly, the "gate-dependent" noise means that the noise channels have the Clifford indices i. Moreover, we refer to the noise as being "constant" in the sense that the noise strength is constant during the RB procedure thus the noise strength parameters δ are omitted. On the contrary, the "stochastic" noise means that the noise channels have the stochastic noise strength δ randomly sampled from a specific distribution. The types of the noise we consider in this chapter are as follows:

Constant noise. $\Lambda_{i,\delta} \equiv \Lambda$. Namely, noise channels are the same for every Clifford gates.
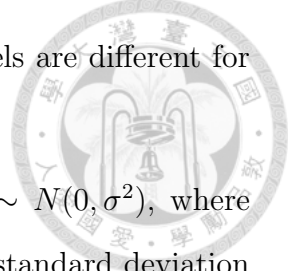
Gate-dependent constant noise. $\Lambda_{i,\delta} \equiv \Lambda_i$. Noise channels are different for each Clifford gates.

Gate-independent stochastic noise. $\Lambda_{i,\delta} \equiv \Lambda_\delta$ with $\delta \sim N(0,\sigma^2)$, where $N(0,\sigma^2)$ denotes the Gaussian distribution with zero mean and standard deviation σ. δ's are independent and identically distributed (i.i.d) Gaussian-distributed parameters and completely uncorrelated between Clifford gates.

Gate-dependent stochastic noise. $\Lambda_{i,\delta}$ with $\delta \sim N(0,\sigma^2)$. δ's are i.i.d Gaussian-distributed parameters and completely uncorrelated between Clifford gates.

Sequence-quasi-static stochastic noise. $\Lambda_{i,\delta}$ with $\delta \sim N(0,\sigma^2)$. δ's are quasi-static at the time-scale of a single RB sequence.

3.1 Randomized Benchmarking for Constant Noise

3.1.1 Constant Noise

Constant noise is the key assumption of the original RB protocol in [5]. In this case, $\Lambda_{i,\delta} \equiv \Lambda$ for every Clifford gates. A single RB sequence with gate length m is

$$\mathcal{S}_{\mathbf{i_m}} = \Lambda \circ \mathcal{C}_{i_{m+1}} \circ \Lambda \circ \mathcal{C}_{i_m} \circ \cdots \Lambda \circ \mathcal{C}_{i_2} \circ \Lambda \circ \mathcal{C}_{i_1}, \tag{3.2}$$

where $\mathbf{i_m}$ is the m-tuple $(i_1, i_2, ..., i_m)$ representing the labels of the randomly chosen Clifford gates and i_{m+1} is uniquely determined by $\mathbf{i_m}$. Define new Clifford gates as follows:

$$\mathcal{G}_{i_j} = \mathcal{C}_{i_j} \circ \cdots \circ \mathcal{C}_{i_1} = \bigcirc_{s=1}^{j} \mathcal{C}_{i_s}, \tag{3.3}$$

where $1 \le j \le (m+1)$. With Eq. (3.3) we can rewrite $\mathcal{C}_{i_j}$ as

$$\mathcal{C}_{i_j} = \mathcal{G}_{i_j} \circ \mathcal{G}_{i_{j-1}}^{\dagger}$$

Thus a single RB sequence becomes

$$
\begin{aligned}
\mathcal{S}_{\mathbf{i_m}} &= \Lambda \circ \mathcal{G}_{i_{m+1}} \circ \mathcal{G}_{i_m}^\dagger \circ \Lambda \circ \mathcal{G}_{i_m} \circ \cdots \circ \mathcal{G}_{i_2}^\dagger \circ \Lambda \circ \mathcal{G}_{i_2} \circ \mathcal{G}_{i_1}^\dagger \circ \Lambda \circ \mathcal{G}_{i_1} \\
&= \Lambda \circ \bigcirc_{s=1}^m (\mathcal{G}_{i_s}^\dagger \circ \Lambda \circ \mathcal{G}_{i_s}),
\end{aligned}
\tag{3.4}
$$

where we have used the fact that $\mathcal{G}_{i_{m+1}} = \bigcirc_{s=1}^{m+1} \mathcal{C}_{i_s} = \mathcal{I}$. Note that if $j \neq k \neq (m+1)$, $\mathcal{C}_{i_j}$ and $\mathcal{C}_{i_k}$ are independent. Since the Clifford gates form a group, $\mathcal{G}_{i_j}$ and $\mathcal{G}_{i_k}$ are independent as well.

Equation (3.4) implies that the average of RB sequences is composed of the m-times product of the independent Clifford twirling of the noise channel Λ with an un-twirled Λ at the end. That is

$$
\mathbb{E}_{\mathbf{i_m} \in \mathbf{I_m}} \mathcal{S}_{\mathbf{i_m}} := \mathcal{S}_m = \Lambda \circ \bigcirc_{s=1}^m (\mathbb{E}_{G \in \mathbf{C}_n}(\mathcal{G}^\dagger \circ \Lambda \circ \mathcal{G})),
\tag{3.5}
$$

where $\mathbf{I_m}$ is the set of all possible m-tuples $\mathbf{i_m}$ and $\mathcal{G}(\rho) = G\rho G^\dagger$. Note that, $\mathcal{S}_m$ is sampled by the k sequences in the RB protocol. As shown in Refs. [33, 34], Haar twirling on a channel Λ produce a depolarizing channel $\mathcal{D}_p$ with the same average gate fidelity as Λ (See Lemma 1 and Appendix A). Since the Clifford twirling is equivalent to the Haar twirling [See Eq. (2.6)], we have

$$
\mathcal{S}_m = \Lambda \circ (\bigcirc_{s=1}^m \mathcal{D}_p).
\tag{3.6}
$$

Thus

$$
\begin{aligned}
P(m) &= \mathrm{Tr}[\mathcal{S}_m(\rho_\psi) E_\psi] = \mathrm{Tr}[\Lambda \circ (\bigcirc_{s=1}^m \mathcal{D}_p)(\rho_\psi) E_\psi] \\
&= \mathrm{Tr}\left[\Lambda \circ (\bigcirc_{s=1}^{m-1} \mathcal{D}_p)\left(p\rho_\psi + \frac{1-p}{2^n} I_n\right) E_\psi\right] \\
&= \mathrm{Tr}\left[\Lambda \circ (\bigcirc_{s=1}^{m-2} \mathcal{D}_p)\left(p^2\rho_\psi + \frac{1-p^2}{2^n} I_n\right) E_\psi\right] \\
&= \mathrm{Tr}\left[\Lambda \left(p^m\rho_\psi + \frac{1-p^m}{2^n} I_n\right) E_\psi\right] \\
&= \mathrm{Tr}[\Lambda(\rho_\psi) E_\psi]p^m + \mathrm{Tr}\left[\Lambda\left(\frac{I_n}{2^n}\right) E_\psi\right](1-p^m) \\
&= Ap^m + B,
\end{aligned}
\tag{3.7}
$$

where

$$A := \text{Tr}\left[\Lambda\left(\rho_\psi - \frac{I_n}{2^n}\right)E_\psi\right]$$
$$B := \text{Tr}\left[\Lambda\left(\frac{I_n}{2^n}\right)E_\psi\right]. \tag{3.8}$$

The explicit form of the fitting parameters A and B indeed absorb the SPAM errors in addition to the un-twirled noise channel from the $(m+1)$-th operation. Note that the decay parameter p we obtained from Eq. (3.7) corresponds to the depolarizing parameter of $\mathcal{D}_p$, which shares the same average gate fidelity as Λ, so we can obtain the average gate fidelity using Eq. (2.10). Hence for the constant noise, RB is able to measure the proper average gate fidelity of the Clifford gates.

3.1.2 Gate-dependent Constant Noise

For the gate-dependent constant noise, $\Lambda_{i,\delta} \equiv \Lambda_i$. This type of noise has been analyzed in [11]. A single RB sequence under this assumption of noise is

$$\mathcal{S}_{\mathbf{i_m}} = \Lambda_{i_{m+1}} \circ \bigcirc_{s=1}^{m}(\mathcal{G}_{i_s}^\dagger \circ \Lambda_{i_s} \circ \mathcal{G}_{i_s}). \tag{3.9}$$

Since the noise channels Λ_{i_s} are dependent with $\mathcal{G}_{i_s}$, Λ_{i_s} cannot be twirled into depolarizing channels. Now consider another possible way to decompose the noisy Clifford gates by transforming a portion of the gate-dependent noise into a gate-independent right channel:

$$\tilde{\mathcal{C}}_i = \Lambda_i \circ \mathcal{C}_i = \mathcal{L}_i \circ \mathcal{C}_i \circ \mathcal{R}, \tag{3.10}$$

where $\mathcal{L}_i$ can be uniquely determined by Λ_i and $\mathcal{R}$. Now the noise channel between two ideal Clifford gates $\mathcal{C}_{i+1}$ and $\mathcal{C}_i$ is $\mathcal{R} \circ \mathcal{L}_i$ instead of Λ_i. Hereafter we abbreviate $\mathcal{R} \circ \mathcal{L}_i$ to $\mathcal{RL}_i$. A single RB sequence becomes

$$\mathcal{S}_{\mathbf{i_m}} = \mathcal{L}_{i_{m+1}} \circ \bigcirc_{s=1}^{m}(\mathcal{G}_{i_s}^\dagger \circ \mathcal{RL}_{i_s} \circ \mathcal{G}_{i_s}). \tag{3.11}$$

13

Thus

$$\mathcal{S}_m = (\mathbb{E}_{G_j \in \mathbf{C}_n} \mathcal{L}_j) \circ \bigcirc_{s=1}^m (\mathbb{E}_{G_i \in \mathbf{C}_n} (\mathcal{G}_i^\dagger \circ \mathcal{R} \mathcal{L}_i \circ \mathcal{G}_i)), \tag{3.12}$$

where the noise decomposition for a Clifford gate $\mathcal{G}_i(\rho) = G_i \rho G_i^\dagger$ is $\tilde{\mathcal{G}}_i = \mathcal{L}_i \circ \mathcal{G}_i \circ \mathcal{R}$ for simplicity. Note that, there are many possible $\mathcal{R}$ can be chosen in Eq. (3.10) to decompose $\tilde{\mathcal{C}}_i$. As shown in Ref. [11], if the noise channel is a CPTP map, there exists a suitable $\mathcal{R}$ such that

$$\mathbb{E}_{G_i \in \mathbf{C}_n} (\mathcal{G}_i^\dagger \circ \mathcal{R} \mathcal{L}_i \circ \mathcal{G}_i) \tag{3.13}$$

produce a depolarizing channel $\mathcal{D}_p$. In this case, RB fitting function becomes [11]

$$P(m) = A p^m + B + \epsilon_m, \tag{3.14}$$

where ϵ_m is the perturbation term that exponentially decreases with m. Instead of finding the suitable $\mathcal{R}$ to obtain the decay parameter p using Eq. (3.13), p can be found by solving the largest eigenvalue of the following $16^n \times 16^n$ matrix for n-qubit system:

$$\mathbb{E}_{G_i \in \mathbf{C}_n} ([\mathcal{G}_i']_{\text{PTM}} \otimes [\tilde{\mathcal{G}}_i]_{\text{PTM}}), \tag{3.15}$$

where $\otimes$ is the matrix tensor product and $\mathcal{G}_i'$ is the unital component of $\mathcal{G}_i$ and is defined to be

$$\mathcal{G}_i'(\rho) = \mathcal{G}_i(\rho - \frac{\text{Tr}(\rho)}{2^n}). \tag{3.16}$$

See Appendix B for the explanations of Wallman's gate-dependent RB theory. Hence for the gate-dependent constant noise, the decay parameter p obtained by RB no longer corresponds to the average gate fidelity. Instead, p is related to the depolarizing channel produced by a special decomposition of the noise channel shown in Eq. (3.13). Note that, for the gate-independent constant noise we have discussed in Sec. 3.1.1, the proper decomposition for producing a depolarizing channel is exactly $\mathcal{R} = \mathcal{I}$ then $\mathcal{L} = \Lambda$.

3.2 Randomized Benchmarking for Stochastic Noise

3.2.1 Gate-independent Stochastic Noise

For the gate-independent stochastic noise, $\Lambda_{i,\delta} \equiv \Lambda_\delta$ with $\delta \sim N(0, \sigma^2)$. Here, the values of the noise parameter δ are completely uncorrelated between distinct Clifford gates in a RB sequence. A single RB sequence in this case is

$$\mathcal{S}_{\mathbf{i_m}, \boldsymbol{\delta_{m+1}}} = \Lambda_{\delta_{m+1}} \circ \bigcirc_{s=1}^{m} (\mathcal{G}_{i_s}^\dagger \circ \Lambda_{\delta_s} \circ \mathcal{G}_{i_s}), \tag{3.17}$$

where $\boldsymbol{\delta_{m+1}}$ is the $(m+1)$-tuple $(\delta_1, \delta_2, ..., \delta_{m+1})$ representing the noise parameters randomly sampled from $N(0, \sigma^2)$ and δ_{m+1} is the noise parameter for the inverse gate at the end of the sequence. For the stochastic noise, the RB sequences not only sample all Clifford gates combination labelled by $\mathbf{i_m}$ but also sample the distribution of noise parameters labelled by $\boldsymbol{\delta_{m+1}}$. Hence we expect that, comparing to the cases of constant noise, relatively more sampling sequences (higher k in the RB protocol) is needed to properly sample $\mathcal{S}_m$. So we can obtain a stable decay curve of the projection state probability under stochastic noise. The average of the RB sequences is

$$\mathcal{S}_m = \mathbb{E}_{\mathbf{i_m} \in \mathbf{I_m}} \int_{-\infty}^{\infty} f(\boldsymbol{\delta_{m+1}}, \boldsymbol{\sigma_{m+1}}) \mathcal{S}_{\mathbf{i_m}, \boldsymbol{\delta_{m+1}}} d\boldsymbol{\delta_{m+1}} \tag{3.18}$$

where $f(\boldsymbol{\delta_{m+1}}, \boldsymbol{\sigma_{m+1}})$ is the probability density function for $\boldsymbol{\delta_{m+1}}$. Since $\delta \sim N(0, \sigma^2)$, $f(\boldsymbol{\delta_{m+1}}, \boldsymbol{\sigma_{m+1}})$ corresponds to the probability density function for the $(m+1)$-dimensional multivariate normal distribution with zero means and the same variance σ in all directions. So $\boldsymbol{\sigma_{m+1}}$ is the $(m+1)$-tuple $(\sigma_1, \sigma_2, ..., \sigma_{m+1})$ with $\sigma = \sigma_1 = \cdots = \sigma_{m+1}$. We can average each noise channel with respect to δ independently,

$$\mathcal{S}_m = \overline{\Lambda} \circ \bigcirc_{s=1}^{m} [\mathbb{E}_{G_i \in \mathbf{C}_n} (\mathcal{G}_i^\dagger \circ \overline{\Lambda} \circ \mathcal{G}_i)], \tag{3.19}$$

where

$$\overline{\Lambda} = \int_{-\infty}^{\infty} f(\delta, \sigma) \Lambda_\delta \, d\delta. \tag{3.20}$$

15

Eq. (3.19) has the same form as Eq. (3.5). Thus RB can properly measure the average gate fidelity of $\overline{\Lambda}$. Hereafter, if a noisy operation $\tilde{\mathcal{U}}$ has stochastic noise with the distribution f, we automatically take the ensemble average of $\tilde{\mathcal{U}}$ with respect to f when considering the average gate fidelity of $\tilde{\mathcal{U}}$.
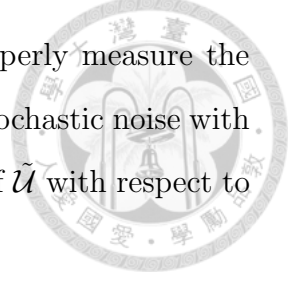
3.2.2 Gate-dependent Stochastic Noise

For gate-dependent stochastic noise, $\tilde{\mathcal{C}}_{i,\delta} = \Lambda_{i,\delta} \circ \mathcal{C}_i$ with $\delta \sim N(0, \sigma^2)$. δ are completely uncorrelated between Clifford gates. We use the same decomposition technique as in Eq. (3.10) with an additional label δ for stochasticity. That is

$$\tilde{\mathcal{C}}_{i,\delta} = \Lambda_{i,\delta} \circ \mathcal{C}_i = \mathcal{L}_{i,\delta} \circ \mathcal{C}_i \circ \mathcal{R}_\delta. \tag{3.21}$$

Then a single RB sequence becomes

$$\mathcal{S}_{\mathbf{i_m},\boldsymbol{\delta_{m+1}}} = \mathcal{L}_{\mathbf{i_{m+1}},\boldsymbol{\delta_{m+1}}} \circ \bigcirc_{s=1}^{m}(\mathcal{G}_{i_s}^\dagger \circ \mathcal{R}_{\delta_s}\mathcal{L}_{i_s,\delta_s} \circ \mathcal{G}_{i_s}). \tag{3.22}$$

This gives the average of the RB sequences as

$$\mathcal{S}_m = (\mathbb{E}_{G_j \in \mathbf{C}_n}\overline{\mathcal{L}_j}) \circ \bigcirc_{s=1}^{m}(\mathbb{E}_{G_i \in \mathbf{C}_n}(\mathcal{G}_i^\dagger \circ \overline{\mathcal{R}\mathcal{L}_i} \circ \mathcal{G}_i)), \tag{3.23}$$

where

$$\begin{aligned} \overline{\mathcal{L}_i} &= \int_{-\infty}^{\infty} f(\delta, \sigma)\mathcal{L}_{i,\delta}\, d\delta, \\ \overline{\mathcal{R}\mathcal{L}_i} &= \int_{-\infty}^{\infty} f(\delta, \sigma)\mathcal{R}_\delta\mathcal{L}_{i,\delta}\, d\delta \end{aligned} \tag{3.24}$$

and the noise decomposition for a Clifford gate $\mathcal{G}_i(\rho) = G_i \rho G_i^\dagger$ is $\tilde{\mathcal{G}_{i,\delta}} = \mathcal{L}_{i,\delta} \circ \mathcal{G}_i \circ \mathcal{R}_\delta$. This is similar to the notation we have used in Eq. (3.12).

Equation (3.23) implies that the gate-dependent RB description we have discussed in Sec. 3.1.2 is still applicable for the gate-dependent stochastic noise. The only difference is that we now consider the ensemble average of the stochastic noise channels instead of the constant noise channels. Inspired by this observation, we assume that the theoretical decay parameter p obtained by RB for the gate-dependent

16

stochastic noise is the largest eigenvalue of the following matrix:

$$\mathbb{E}_{G_i \in \mathbf{C}_n}([\mathcal{G}'_i]_{\mathrm{PTM}} \otimes [\tilde{\mathcal{G}}_{i,\mathrm{ave}}]_{\mathrm{PTM}}), \tag{3.25}$$

where

$$\tilde{\mathcal{G}}_{i,\mathrm{ave}} = \int_{-\infty}^{\infty} f(\delta, \sigma) \tilde{\mathcal{G}}_{i,\delta} \, d\delta. \tag{3.26}$$

3.2.3 Sequence-quasi-static Stochastic Noise

In this section, we consider the stochastic noise with maximum non-Markovianity during the RB procedure, which means that $\delta \sim N(0, \sigma^2)$ are quasi-static at the time-scale of a single RB measurement.

A single RB sequence in this case is similar to the case of gate-dependent constant noise but with an additional noise parameter δ for all the noise channels in the sequence,

$$\mathcal{S}_{\mathbf{i_m},\delta} = \mathcal{L}_{i_{m+1},\delta} \circ \bigcirc_{s=1}^{m}(\mathcal{G}_{i_s}^{\dagger} \circ \mathcal{R}_\delta \mathcal{L}_{i_s,\delta} \circ \mathcal{G}_{i_s}). \tag{3.27}$$

Thus RB sequences actually sample the average of the constant gate-dependent average sequence given by Eq. (3.12) with respect to the distribution of δ. That is

$$\mathcal{S}_m = \int_{-\infty}^{\infty} f(\delta, \sigma) \left(\mathbb{E}_{G_j \in \mathbf{C}_n} \mathcal{L}_{j,\delta}\right) \circ \bigcirc_{s=1}^{m}(\mathbb{E}_{G_i \in \mathbf{C}_n}(\mathcal{G}_i^{\dagger} \circ \mathcal{R}_\delta \mathcal{L}_{i,\delta} \circ \mathcal{G}_i)) \, d\delta, \tag{3.28}$$

which implies that the projection state probabilities obtained from the RB procedure is composed of the projection state probabilities which correspond to different noise parameters, denoted $P(m, \delta)$. $P(m, \delta)$'s distribute the same as δ's. Based on this observation and Eq. (3.14), the probability density function (PDF) RB fitting formula for sequence-quasi-static stochastic noise is

$$P(m) = \int_{-\infty}^{\infty} f(\delta, \sigma) P(m, \delta) \, d\delta = A \left[\int_{-\infty}^{\infty} f(\delta, \sigma) p_\delta^m \, d\delta \right] + B + \epsilon_m, \tag{3.29}$$

where p_δ is the largest eigenvalue of the the following $16^n \times 16^n$ matrix for n-qubit

system:

$$\mathbb{E}_{G_i \in \mathbf{C}_n}([\mathcal{G}'_i]_{\text{PTM}} \otimes [\tilde{\mathcal{G}}_{i,\delta}]_{\text{PTM}}). \qquad (3.30)$$

Here, $\tilde{\mathcal{G}}_{i,\delta} \equiv \Lambda_{i,\delta} \circ \mathcal{G}_i$ is the noisy Clifford gate $\mathcal{G}_i$ with the noise parameter δ. At first glance, Eq. (3.29) looks intimidating to use for fitting the projection state probabilities. However, once we determine the dominant non-Markovian noise model, we can calculate p_δ theoretically for any δ and then carry out the integral discretely. Note that, we do not fit the decay parameters p_δ in Eq. (3.29). Instead, we fit the best-suited sequence-quasi-static stochastic noise to describe the non-Markovian noise of the gate-based quantum computing device. Since $\delta \sim N(0, \sigma^2)$, the parameter we try to fit here is the standard deviation σ. In this situation, the physical interpretation of the RB fitting result is clear: σ corresponds to the best-suited normal distribution to describe the non-Markovian noise affecting the tested qubits.

Chapter 4

Simulation Methods

This chapter introduces the simulation methods and models we use for the RB procedure. All the simulations are done with Python. Several assumptions and revisions are made in our RB simulations for simplicity and efficiency. We assume that there are no SPAM errors to highlight the effect of the gate errors. We also assume that the final inverse gate is perfect for convenience. These assumptions do not affect the decay behavior of the projection state probabilities. Our steps for the RB simulations are as follows.

1. Pick a set of Clifford gate lengths $(m_1, m_2, ..., m_l)$ with $m_1 < m_2 < ... < m_l$, where l is the number of the data points for the RB function fitting. So m_l is the maximum gate length of the RB sequences.

2. Generate k sequences consisting of m_l quantum operations without the inverse operation. These m_l operations are randomly chosen from $\mathbf{C}_n$ and are generated with noise.

3. Preparing the initial state ρ_ψ. We set the initial state as $|\psi\rangle = |0\rangle$ and assume the ideal state preparation. So $\rho_0 = |0\rangle \langle 0|$.

4. Operate the first m_1 operations in the sequences from step 2 on ρ_0 then operate the perfect inverse gate of these m_1 operations to get the final states ρ_0'.

5. Apply the perfect POVM measurements $E_0 = |0\rangle \langle 0|$. Measure the projection

state probability $P(m_1) = \text{Tr}(E_0 \rho_0')$ by averaging over the measurement results from the k sequences.
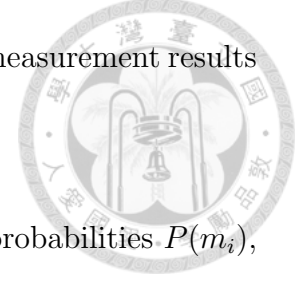
6. Repeat steps 3-5 for $m_2, ..., m_l$ to get the projection state probabilities $P(m_i)$, where $1 \leq i \leq l$. Here we use the same k sequences generated in step 2 for different m_i.

7. Fit the dataset $[m_i, P(m_i)]$ with Eq. (3.1) for gate-independent noise and Eq. (3.14) for gate-dependent noise to measure the dacay parameter p, then use Eq. (2.10) to obtain the Clifford fidelity. Fit the dataset $[m_i, P(m_i)]$ with Eq. (3.29) for sequence-quasi-static noise. We neglect the purtubation terms ϵ_m in Eq. (3.14) and (3.29). We also bound $B = 0.5$ for the single-qubit model and $B = 0.25$ for the two-qubit model to ensure the fitting functions end up decay to the projection state probability of the maximally mixed state.

4.1 Single-qubit Simulation Model

In our single-qubit RB simulations, we use the decomposition table of the single-qubit Clifford group $\mathbf{C}_1$ in Ref. [2] (See Table 4.1). The generators of $\mathbf{C}_1$ are $\{X_{\pm\pi/2}, Z_{\pm\pi/2}\}$. We assume that there is no noise on the $Z_{\pm\pi/2}$ gates since rotations around Z axis can be implemented perfectly by virtual-Z gates without applying actual pulses for various quantum computing systems[35]. Hence $Z_{\pm\pi/2}$ are executed by perfect unitary operations. The $X_{\pm\pi/2}$ gates are generated by the on-resonance Hamiltonian with dephasing noise:

$$\tilde{H} = \frac{1}{2}X + \frac{1}{2}\delta Z, \tag{4.1}$$

where δ denotes the dephasing noise strength. The simulation calculates noisy gates $\tilde{X}_{\pm\pi/2}$ by taking the product of the time-sliced propagators during the conditional $\pi/2$-pulse duration. Let $T_{\pi/2}$ be the conditional $\pi/2$-pulse time and Δ be the number

Gate numbering	X/Z generation
1	$X, -X$
2	X^2
3	$-Z, X^2, Z$
4	X, Z^2, X
5	$X, -Z, X, Z$
6	$X, Z, X, -Z$
7	$-X, -Z, X, Z$
8	$-X, Z, X, -Z$
9	$-Z, X, Z, X$
10	$-Z, X, Z, -X$
11	$Z, X, -Z, X$
12	$Z, X, -Z, -X$
13	$-Z, X, Z, X, -Z$
14	$Z, -X, -Z, -X, Z$
15	$X, Z, -X$
16	$X, -Z, -X$
17	$-X, Z^2, -X, -Z$
18	$-X, -Z^2, -X, Z$
19	$X, -Z, X$
20	X, Z, X
21	$-Z, X, Z, X, Z$
22	$-Z, X, Z, -X, -Z$
23	X^2, Z
24	$-X^2, -Z$

Table 4.1: **The decomposition table of the single-qubit Clifford group** [2]. $(-)K$ and $(-)K^2$ denote $K_{\pm\pi/2}$ and $K_{\pm\pi}$ gates ($K = X, Y, Z$) respectively.

of the time slices. Then $dt = T_{\pi/2}/\Delta$. Thus we have

$$\tilde{X}_{\pm\pi/2} = \prod_{t=0}^{T_{\pi/2}} e^{\mp i\tilde{H}dt}, \tag{4.2}$$

where $T_{\pi/2} = \pi/2$. We set $\Delta = 1000$.

Note that, the single-qubit Clifford gates are composed of two $X_{\pm\pi/2}$ gates and different numbers of the $Z_{\pm\pi/2}$ gates. Although every Clifford gate has the same operation time $2T_{\pi/2}$, the noise is still gate-dependent because of the different interleaved $Z_{\pm\pi/2}$ gates. The theoretical noise channels for the Clifford gates are unitary and can be obtained explicitly in matrix forms. Consider the decomposition of the

$\tilde{X}_{\pm\pi/2}$ gates:

$$\tilde{X}_{\pm\pi/2} = \cos\left(\frac{\pi}{4}\zeta\right)I \mp i\sin\left(\frac{\pi}{4}\zeta\right)\left(\frac{1}{\zeta}X + \frac{\delta}{\zeta}Z\right), \qquad (4.3)$$

where $\zeta := \sqrt{1 + \delta^2}$. The Pauli matrices satisfy the identity

$$\cos\frac{\phi}{2}I \mp i\sin\frac{\phi}{2}(\cos\gamma X + \sin\gamma Z) = Y_{\mp\gamma}X_{\pm\phi}Y_{\pm\gamma}. \qquad (4.4)$$

Applying Eq. (4.3) and Eq. (4.4) to the decomposition of the Clifford gates gives the theoretical noise channels. For example, $\tilde{C}_1$ can be decomspoed into

$$
\begin{aligned}
\tilde{C}_1 = \tilde{X}_{\pi/2}\tilde{X}_{-\pi/2} &= (Y_{-\gamma}X_{\pi\zeta/2}Y_\gamma)(Y_\gamma X_{-\pi\zeta/2}Y_{-\gamma}) \\
&= Y_{-\gamma}X_{\pi\zeta/2}Y_{2\gamma}X_{-\pi\zeta/2}Y_{-\gamma}(C_1^\dagger C_1),
\end{aligned}
\qquad (4.5)
$$

where $\cos\gamma = 1/\zeta$ and $\sin\gamma = \delta/\zeta$. Hence $\tilde{\mathcal{C}}_1 = \Lambda_{1,\delta} \circ \mathcal{C}_1$ with $\Lambda_{1,\delta}(\rho) = U_{1,\delta}\rho U_{1,\delta}^\dagger$. Here

$$U_{1,\delta} = Y_{-\gamma}X_{\pi\zeta/2}Y_{2\gamma}X_{-\pi\zeta/2}Y_{-\gamma}C_1^\dagger. \qquad (4.6)$$

Note that, ζ and γ are determined from the dephasing noise strength δ. When $\delta = 0$, the noise channels of C_i reduce to $\Lambda_{i,\delta=0} = \mathcal{I}$.

4.2 Two-qubit Simulation Model

4.2.1 Effective Hamiltonian and Microwave Pulses

Our two-qubit model simulates the real quantum computing experiment with silicon-based quantum-dot spin qubits. We use the experimental parameters of the silicon-metal-oxide-semiconductor (silicon-MOS) double-quantum-dot device in Ref. [1]. The device is in the $(n_1, n_2) = (1, 1)$ charge stability region. That is, a single electron on each dot denoted by Q1 and Q2 respectively. The Hamiltonian in the

two-spin basis $(\uparrow\uparrow, \uparrow\downarrow, \downarrow\uparrow, \downarrow\downarrow)$ can be approximated as

$$H = \frac{1}{2} \begin{pmatrix} 2\overline{E}_Z & \gamma_2 B_1 & \gamma_1 B_1 & 0 \\ \gamma_2 B_1^* & \delta E_Z - J & J & \gamma_1 B_1 \\ \gamma_1 B_1^* & J & -\delta E_Z - J & \gamma_2 B_1 \\ 0 & \gamma_1 B_1^* & \gamma_2 B_1^* & -2\overline{E}_Z \end{pmatrix}. \tag{4.7}$$

Here, γ_1 (or γ_2) is the gyromagnetic ratio of Q1 (or Q2) that couples qubits to the oscillating AC magnetic field B_1 created by the electron spin resonance (ESR) wire, J is the exchange coupling, $\overline{E}_Z$ is the average Zeeman energy, and δE_Z is the difference in Zeeman energies between the two dots. Equation (4.7) can be written in the new basis $(\uparrow\uparrow, \tilde{\uparrow\downarrow}, \tilde{\downarrow\uparrow}, \downarrow\downarrow)$ that diagonalizes the Hamiltonian when the AC magnetic field is absence. That is

$$H = \frac{1}{2} \begin{pmatrix} 2\overline{E}_Z & \gamma_{2\uparrow} B_1 & \gamma_{1\uparrow} B_1 & 0 \\ \gamma_{2\uparrow} B_1^* & \delta\tilde{E}_Z - J & 0 & \gamma_{1\downarrow} B_1 \\ \gamma_{1\uparrow} B_1^* & 0 & -\delta\tilde{E}_Z - J & \gamma_{2\downarrow} B_1 \\ 0 & \gamma_{1\downarrow} B_1^* & \gamma_{2\downarrow} B_1^* & -2\overline{E}_Z \end{pmatrix}, \tag{4.8}$$

where $\gamma_{n\uparrow}$ (or $\gamma_{n\downarrow}$) is the effective gyromagnetic ratio that couples qubit n to the oscillating magnetic field B_1 when the other qubit is in the $|\uparrow\rangle$ (or $|\downarrow\rangle$) state, $\delta\tilde{E}_Z = \sqrt{\delta E_Z^2 + J^2}$, and

$$\begin{aligned} \left|\tilde{\downarrow\uparrow}\right\rangle &= \cos\frac{\theta}{2} |\downarrow\uparrow\rangle + \sin\frac{\theta}{2} |\uparrow\downarrow\rangle, \\ \left|\tilde{\uparrow\downarrow}\right\rangle &= -\sin\frac{\theta}{2} |\downarrow\uparrow\rangle + \cos\frac{\theta}{2} |\uparrow\downarrow\rangle. \end{aligned} \tag{4.9}$$

Here

$$\begin{aligned} \cos\frac{\theta}{2} &= \frac{\delta E_Z + \delta\tilde{E}_Z}{\sqrt{(\delta E_Z + \delta\tilde{E}_Z)^2 + J^2}}, \\ \sin\frac{\theta}{2} &= \frac{J}{\sqrt{(\delta E_Z + \delta\tilde{E}_Z)^2 + J^2}}. \end{aligned} \tag{4.10}$$

Thus the effective gyromagnetic ratios follow the rotation:

$$\gamma_{1\uparrow} = \gamma_1 \cos \frac{\theta}{2} - \gamma_2 \sin \frac{\theta}{2},$$
$$\gamma_{1\downarrow} = \gamma_1 \cos \frac{\theta}{2} + \gamma_2 \sin \frac{\theta}{2},$$
$$\gamma_{2\uparrow} = \gamma_2 \cos \frac{\theta}{2} + \gamma_1 \sin \frac{\theta}{2},$$
$$\gamma_{2\downarrow} = \gamma_2 \cos \frac{\theta}{2} - \gamma_1 \sin \frac{\theta}{2}.$$

(4.11)

The system parameters are provided in Ref. [1]:

$$\overline{E}_Z/h = 39.33 \text{ GHz},$$

$$\delta E_Z/h = 13.26 \text{ MHz},$$

$$J/h = 1.59 \text{ MHz},$$

where h is Planck's constant. In our two-qubit simulations, we use the Hamiltonian described by Eq. (4.8) in the basis $(\uparrow\uparrow, \tilde{\uparrow\downarrow}, \tilde{\downarrow\uparrow}, \downarrow\downarrow)$ and neglect the rapidly oscillation terms which include $\overline{E}_Z$. Hence the Hamiltonian for our two-qubit simulations is

$$H = \frac{1}{2} \begin{pmatrix} 0 & \gamma_{2\uparrow}B_1 & \gamma_{1\uparrow}B_1 & 0 \\ \gamma_{2\uparrow}B_1^* & \delta\tilde{E}_Z - J & 0 & \gamma_{1\downarrow}B_1 \\ \gamma_{1\uparrow}B_1^* & 0 & -\delta\tilde{E}_Z - J & \gamma_{2\downarrow}B_1 \\ 0 & \gamma_{1\downarrow}B_1^* & \gamma_{2\downarrow}B_1^* & 0 \end{pmatrix}.$$

(4.12)

Note that, we have not considered the noise model for RB simulations so far.

The four resonance frequencies of the Hamiltonian described in Eq. (4.12) are defined as

$$f_{1\uparrow} = \frac{\delta\tilde{E}_Z + J}{2h},$$
$$f_{1\downarrow} = \frac{\delta\tilde{E}_Z - J}{2h},$$
$$f_{2\uparrow} = \frac{-\delta\tilde{E}_Z + J}{2h},$$
$$f_{2\downarrow} = \frac{-\delta\tilde{E}_Z - J}{2h}.$$

(4.13)

To perform Rabi rotations, It is more convenient to describe the system Hamiltonian in a time-dependent rotating frame (See Appendix C). That is defined as

$$H' = RHR^\dagger + i\frac{\partial R}{\partial t}R^\dagger, \qquad (4.14)$$

with a rotating diagonal matrix $R = \text{diag}\{1, e^{i\omega_{1\downarrow}t}, e^{-i\omega_{1\uparrow}t}, 1\}$. We define $\omega_{**} = 2\pi f_{**}$ as the resonance angular frequencies, where $** = 1\uparrow, 1\downarrow, 2\uparrow$, or $2\downarrow$. Applying Eq. (4.14) to the Hamiltonian in Eq. (4.12), we get

$$H' = \frac{1}{2}\begin{pmatrix} 0 & \gamma_{2\uparrow}B_1 e^{i\omega_{2\uparrow}t} & \gamma_{1\uparrow}B_1 e^{i\omega_{1\uparrow}t} & 0 \\ \gamma_{2\uparrow}B_1^* e^{-i\omega_{2\uparrow}t} & 0 & 0 & \gamma_{1\downarrow}B_1 e^{i\omega_{1\downarrow}t} \\ \gamma_{1\uparrow}B_1^* e^{-i\omega_{1\uparrow}t} & 0 & 0 & \gamma_{2\downarrow}B_1 e^{i\omega_{2\downarrow}t} \\ 0 & \gamma_{1\downarrow}B_1^* e^{-i\omega_{1\downarrow}t} & \gamma_{2\downarrow}B_1^* e^{-i\omega_{2\downarrow}t} & 0 \end{pmatrix}. \qquad (4.15)$$

Hence in the rotating frame, the Hamiltonian with excitation frequency $f_{n\uparrow}$ (or $f_{n\downarrow}$) applied by B_1 produces conditional Rabi rotation on qubit n when the other qubit is in the $|\uparrow\rangle$ (or $|\downarrow\rangle$) state. Take $B_1(t) = (\Omega/\gamma_{1\uparrow})e^{-i\omega_{1\uparrow}t}$ as an example. After neglecting the far off-resonance terms and approximating $\gamma_{1\downarrow} \approx \gamma_{1\uparrow}$, the Hamiltonian in the rotating frame can be written as

$$H_{\text{RWA}}^{1\uparrow} = \frac{1}{2}\begin{pmatrix} 0 & 0 & \Omega & 0 \\ 0 & 0 & 0 & 0 \\ \Omega & 0 & 0 & 0 \\ 0 & 0 & 0 & 0 \end{pmatrix} + \frac{1}{2}\begin{pmatrix} 0 & 0 & 0 & 0 \\ 0 & 0 & 0 & \Omega e^{-i(J/\hbar)t} \\ 0 & 0 & 0 & 0 \\ 0 & \Omega e^{i(J/\hbar)t} & 0 & 0 \end{pmatrix}. \qquad (4.16)$$

Here, the "RWA" subscript implies that we have already done the rotating-wave approximation. The time evolution of the first term gives the microwave pulse that rotates Q1 when Q2 is in the $|\uparrow\rangle$ state. The second term is the crosstalk error, which results in finite rotations and phase shifts in the off-resonance states. To cancel out the crosstalk error, the lengths and amplitudes of all conditional $\pi/2$-pulses are chosen such that the off-diagonal component of the second term is 0 after

a conditional $\pi/2$-pulse time (See Supplementary Information of Ref. [1]),

$$T_{\pi/2} = \frac{h}{4\Omega} = \frac{h\sqrt{16n^2 - \frac{\gamma_{1\uparrow}}{\gamma_{1\downarrow}}}}{4J} \approx \frac{h\sqrt{16n^2 - 1}}{4J}, \tag{4.17}$$

where we set $n = 1$ in our simulations. So only the phase error on the diagonal components is left. Then the phase error can be almost perfectly canceled by applying the virtual-phase gates to future pulses. See Appendix D.

As mentioned before, our two-qubit simulations are executed in the basis ($\uparrow\uparrow$, $\tilde{\uparrow\downarrow}$, $\tilde{\downarrow\uparrow}$, $\downarrow\downarrow$) with the Hamiltonian described in Eq. (4.12). We set the evolution time at $T_{\pi/2} = h/4\Omega \approx 610$ ns for all the conditional Rabi rotations to get the conditional $\pi/2$-pulses. Then we assume the dephasing noise with equal strength δ on Q1 and Q2. Thus the noisy Hamiltonian is

$$\tilde{H} = \frac{1}{2} \begin{pmatrix} 0 & \gamma_{2\uparrow}B_1 & \gamma_{1\uparrow}B_1 & 0 \\ \gamma_{2\uparrow}B_1^* & \delta\tilde{E}_Z - J & 0 & \gamma_{1\downarrow}B_1 \\ \gamma_{1\uparrow}B_1^* & 0 & -\delta\tilde{E}_Z - J & \gamma_{2\downarrow}B_1 \\ 0 & \gamma_{1\downarrow}B_1^* & \gamma_{2\downarrow}B_1^* & 0 \end{pmatrix} + \delta(Z_1 \otimes Z_2), \tag{4.18}$$

where Z_1 (or Z_2) is the Pauli Z operator on Q1 (or Q2). The explicit form of the conditional $\pi/2$-pulses in our simulations are

$$U_{**}^{\pm\pi/2} = \prod_{t=t_i}^{t_i+T_{\pi/2}} e^{-i\tilde{H}(t)dt/\hbar}, \tag{4.19}$$

where we set the time resolution $dt = 5$ ns, and the oscillating magnetic fields B_1 corresponding to different resonance frequencies are written as

$$B_1(t) = \frac{\Omega}{\gamma_{**}}e^{-i(\omega_{**}t+\phi)}. \tag{4.20}$$

Here, $\Omega/h = 410$ kHz is the Rabi frequency, ϕ is the phase offset of the AC magnetic field. The phase offset of the oscillating magnetic field B_1 is set to $\phi = 0$ (or $\phi = \pi$) for $\pi/2$ (or $-\pi/2$) conditional pulses.

Number of Generators	Number of Clifford gates
0	16
1	384
2	4176
3	6912
4	32
Total	11520

Table 4.2: **Number of Clifford gates built from different number of generators** [1]. We do not include virtual-$Z_{\pi/2}$ gates in the generators in this table since they require no pulse time to operate. The 16 Clifford gates with 0 generators are all combined by virtual-$Z_{\pi/2}$ gates only.

4.2.2 Clifford Gate Decomposition and Noise Channel Extraction

The generators of the two-qubit Clifford group $\mathbf{C}_2$ are combined by two conditional $\pi/2$-pulses each and are defined as follows:

$$
\begin{aligned}
[X_{\pi/2}]_n &= U_{n\uparrow}^{\pi/2} U_{n\downarrow}^{\pi/2} \\
[X_{\pi/2} + CROT]_n &= U_{n\uparrow}^{\pi/2} U_{n\downarrow}^{-\pi/2} \\
[Z - CROT]_n &= U_{n\uparrow}^{\pi/2} U_{n\uparrow}^{\pi/2} \\
[CROT]_n &= U_{n\downarrow}^{-\pi/2} U_{n\downarrow}^{-\pi/2}
\end{aligned}
, \tag{4.21}
$$

where $n = 1, 2$ labels the target qubit of the conditional $\pi/2$-pulses. These 8 generators along with the virtual-$Z_{\pi/2}$ gates acting on Q1 and Q2 generate all the 11520 elements in $\mathbf{C}_2$. See Table 4.2.

We calculate gate-dependent unitary noise channels $\tilde{\mathcal{C}}_i = \Lambda_{i,\delta} \circ \mathcal{C}_i$ resulted from the Hamiltonian dephasing noise $\delta \left(Z_1 \otimes Z_2 \right)$ by decomposing conditional $\pi/2$-pulses into blocks of effective one-qubit operators. Take $U_{1\uparrow}^{\pi/2}$ as an example. Here we do not consider the crosstalk error since it can be compensated by virtual-phase rotations (See Appendix D). The noisy Hamiltonian for $U_{1\uparrow}^{\pi/2}$ without the crosstalk

terms in the rotating frame is

$$\tilde{H}^{1\uparrow}_{\text{RWA}} = \frac{1}{2} \begin{pmatrix} 2\delta & 0 & \Omega & 0 \\ 0 & -2\delta & 0 & 0 \\ \Omega & 0 & -2\delta & 0 \\ 0 & 0 & 0 & 2\delta \end{pmatrix}. \tag{4.22}$$

The subblock in the basis $(\uparrow\uparrow, \tilde{\downarrow\uparrow})$ is equivalent to $X_{\pi/2}$ rotation with dephasing noise. Using Eq. (4.4) we get

$$\tilde{X}_{\pi/2} = Y_{-\gamma} X_{\pi\zeta/2} Y_{\gamma}. \tag{4.23}$$

Define $\delta' = 2\delta/\Omega$. Here, $\zeta := \sqrt{1 + \delta'^2}$, $\cos\gamma = 1/\zeta$, and $\sin\gamma = \delta'/\zeta$. The subblock in the basis $(\tilde{\uparrow\downarrow}, \downarrow\downarrow)$ simply gives $Z_{-\pi\delta'/2}$. We decompose every conditional $\pi/2$-pulse in order to obtain its noise operators in the form of 4×4 matrices. After that, we can construct the unitary noise channel $\Lambda_{i,\delta}$ for every two-qubit Clifford gate using the same method as described in Eq. (4.6).

Chapter 5

Results and Discussions

In this chapter, we discussed the RB simulation results with different types of noises. The single-qubit simulations are executed with time resolution $dt = T_{\pi/2}/1000$ and the number of RB sequences $k = 500$. For the two-qubit simulations, $dt = 5$ ns and $k = 1000$.

5.1   RB Simulations with Constant Noise

5.1.1   Hamiltonian Noise and Channel Noise

In this section, we compare the Clifford fidelity obtained from RB under different sources of constant dephasing noise in the one-qubit model. The Hamiltonian dephasing noise with noise strength δ is already defined in Eq. (4.1):

$$\tilde{H} = \frac{1}{2}X + \frac{1}{2}\delta Z. \tag{5.1}$$

For every Clifford gate C_i, the channel dephasing noise is defined as a perfect Clifford gate followed by a unitary Z-rotation,

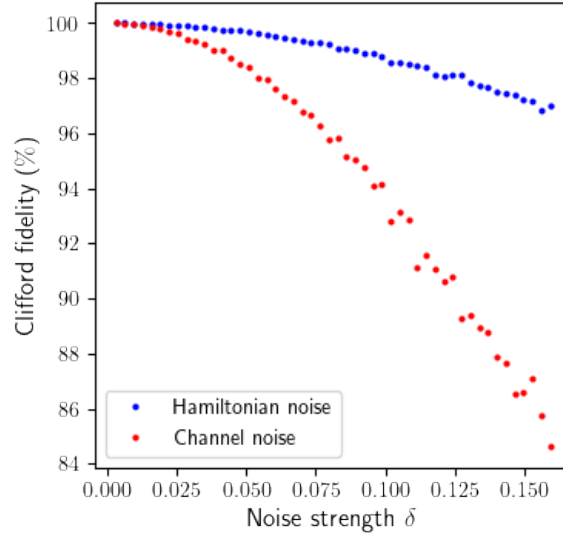$$\tilde{C}_i = Z_\theta C_i. \tag{5.2}$$

Figure 5.1: **Clifford fidelity of channel noise and Hamiltonian noise in the single-qubit model.** Channel noise and Hamiltonian noise with strength δ are defined in Eq. (5.1) and Eq. (5.2) respectively. The Clifford fidelity for different δ is obtained from RB procedure implemented with the single-qubit model.

Since each Clifford gate is combined by two noisy $X_{\pm\pi/2}$ gates and different numbers of perfect $Z_{\pm\pi/2}$ gates (See Table 4.1), we set $\theta = 2T_{\pi/2}\delta = \pi\delta$ to make the strength of the channel noise similar to the Hamiltonian noise.

The RB simulation result shows that the Clifford fidelities under the channel noise are smaller than those under the Hamiltonian noise (See Fig. 5.1). This is because the channel noise is in the same Z direction while Hamiltonian noise is mixed by the time evolution of the Hamiltonian. Thus channel noise leads to more noise accumulations. This implies that the simple channel noise models often used in the RB theories cannot simulate the behavior of the Hamiltonian noise. Moreover, the channel noise cannot describe the gate-independency of noise naturally induced from the Clifford decomposition of the generators. These are our intuitions for using Hamiltonian noise models to analyze RB.

5.1.2 Hamiltonian Constant Dephasing Noise

In this section, we compare the Clifford fidelity obtained from RB with the theoretical average gate fidelity under gate-dependent constant noise. The noise gate-dependency is caused by the different decompositions for different Clifford gates
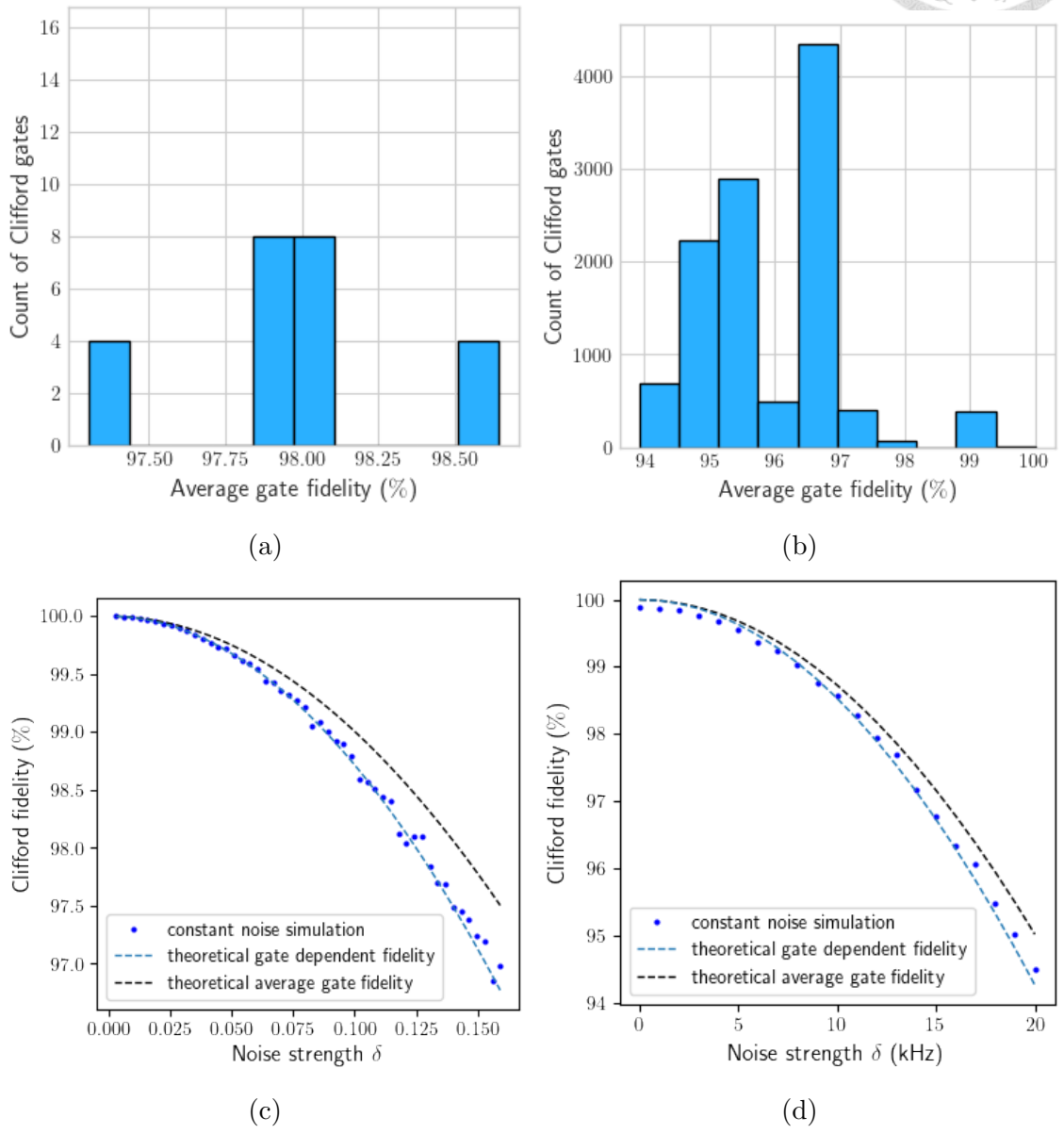
Figure 5.2: **Hamiltonian constant dephasing noise simulations.** The histogram of the average gate fidelities for **(a)** single-qubit model ($\delta = 0.143$) and **(b)** two-qubit model ($\delta = 18\,\mathrm{kHz}$). RB simulation results using **(c)** single-qubit model and **(d)** two-qubit model. Hamiltonian dephasing noise is constant with strength δ during the RB procedure. The blue dashed line is calculated using Eq. (3.15). And the black dashed line is defined in Eq. (5.3).

[See Fig. 5.2 (a) and 5.2 (b)]. The theoretical average gate fidelity under the gate-dependent constant noise is defined as

$$F_{\text{thr}} = \mathbb{E}_{C \in \mathbf{C}_n} F_{\text{ave}}(\tilde{\mathcal{C}}, \mathcal{C}). \qquad (5.3)$$

F_{thr} includes the average gate fidelities $F_{\text{ave}}(\tilde{\mathcal{C}}, \mathcal{C})$ of the Clifford gates thus is a reasonable number to evaluate the average performance of the unitary operations. Note that, F_{thr} reduces to the average gate fidelity of a single noise channel when the noise is gate-independent.

The simulation results shows that [See Fig. 5.2 (c) and 5.2 (d)] the fidelity obtained from RB meets the gate dependent fidelity defined with Eq. (3.13) and (3.15), thus verifying the analysis of RB with gate-dependent constant noise in Ref. [11]. RB cannot measure F_{thr} properly. In fact, RB underestimates F_{thr} in both single-qubit and two-qubit simulations, which means that the depolarizing parameter of the depolarizing channel produced in Eq. (3.13) is greater than the average of the depolarizing parameters corresponding to the distinct Clifford-twirled noise channels. Namely,

$$p\left[\mathbb{E}_{G_i \in \mathbf{C}_n}(\mathcal{G}_i^\dagger \circ \mathcal{R}\mathcal{L}_i \circ \mathcal{G}_i)\right] > \mathbb{E}_{C_i \in \mathbf{C}_n}\left\{p\left[\mathbb{E}_{G_j \in \mathbf{C}_n}(\mathcal{G}_j^\dagger \circ \Lambda_i \circ \mathcal{G}_j)\right]\right\}. \qquad (5.4)$$

Here, $\tilde{\mathcal{C}}_i = \Lambda_i \circ \mathcal{C}_i = \mathcal{L}_i \circ \mathcal{C}_i \circ \mathcal{R}$.

5.2   RB Simulations with Stochastic Noise

In this section, we discuss the Hamiltonian dephasing noise with time-varying δ. The noise strength δ is sampled from a Gaussian distribution with zero-mean and standard deviation σ. We define the noise changing time T_σ as the period with the same δ in the system. In other words, δ changes after every T_σ. The minimum can be set to $T_\sigma = T_{\pi/2}$ (change per $\pi/2$-pulse time), and the maximum can be set to $T_\sigma = T_{\text{seq}}$ (change per RB sequence, which is the sequence-quasi-static noise).

32

5.2.1 Hamiltonian Stochastic Dephasing Noise
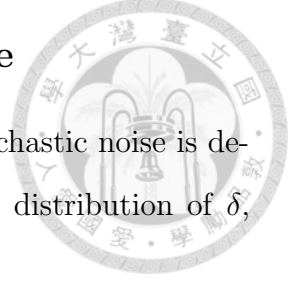
The theoretical average gate fidelity with gate-dependent stochastic noise is defined as the ensemble average of Eq. (5.3) with respect to the distribution of δ,

$$F_{\text{thr}} = \int_{-\infty}^{\infty} f(\delta, \sigma) \mathbb{E}_{C \in \mathbf{C}_n} F_{\text{ave}}(\tilde{\mathcal{C}}(\delta), \mathcal{C}) \, d\delta. \tag{5.5}$$

We choose $T_\sigma = 2T_{\pi/2}$ for the single-qubit simulation because every Clifford gate has the same operation time $2T_{\pi/2}$. Thus the noise with $T_\sigma = 2T_{\pi/2}$ meets the gate-dependent stochastic RB analysis in Sec. 3.2.2. While for the two-qubit simulation, the operation times of the Clifford gates are different. Since the decomposition table results an average of 5.14 $\pi/2$-pulses per Clifford gate (See Table 4.2), we choose $T_\sigma = 5.14T_{\pi/2}$ to approximate the stochastic noise changing per Clifford gate.

Both single-qubit and two-qubit simulations show that, unlike the cases of constant noise, what RB measures is almost identical to the theoretical average gate fidelity with stochastic noise [See the blue and the black dashed curves in Fig. 5.3 (c) and Fig. 5.3 (d)]. The distributions of the noise average gate fidelities resulting from the distributions of δ are similar between distinct Clifford gates. When σ is small, such gate-dependent distribution of average gate fidelities is almost indistinguishable (See Fig. 5.4). The stochasticity of noise decreases the effect of gate-dependency. According to the simulation results, if the stochastic gate-dependent noise is Gaussian distributed, RB can still properly measure the average gate fidelity in a reasonable range of noise strength. We believe that this inference is also applicable for other noise distributions with not-too-large probability density variations for different Clifford gates.

It turns out that Eq. (3.25) still works well to predict the simulation result [See the blue dots and the blue dashed curves in Fig. 5.3 (c) and Fig. 5.3 (d)]. Besides, we also do the simulation with the fastest changing noise we consider here by setting $T_\sigma = T_{\pi/2}$. The result implies that the fidelities with faster T_σ are higher than those with slower T_σ. We believe that rapidly changing noise is more random during a single RB sequence. Thus it is harder for the fast noise to accumulate large
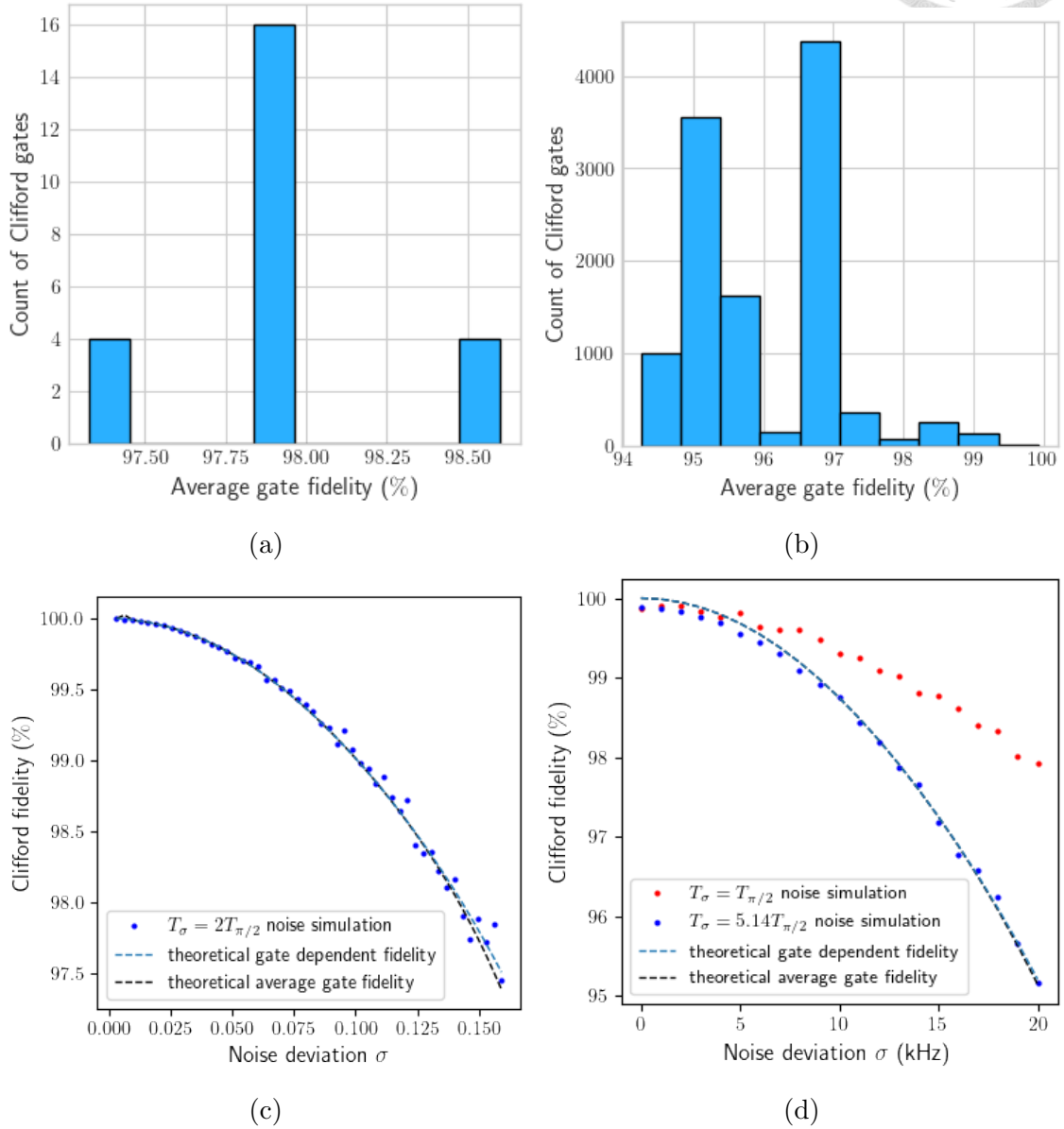
Figure 5.3: **Hamiltonian stochastic dephasing noise simulations.** The histogram of the average gate fidelities for **(a)** single-qubit model ($\sigma = 0.143$) and **(b)** two-qubit model ($\sigma = 18\,\mathrm{kHz}$). RB simulation results using **(c)** single-qubit model and **(d)** two-qubit model. The blue dashed line is calculated using Eq. (3.25). And the black dashed line is defined in Eq. (5.5). All the integrals with respect to the distribution of δ are calculated discretely.
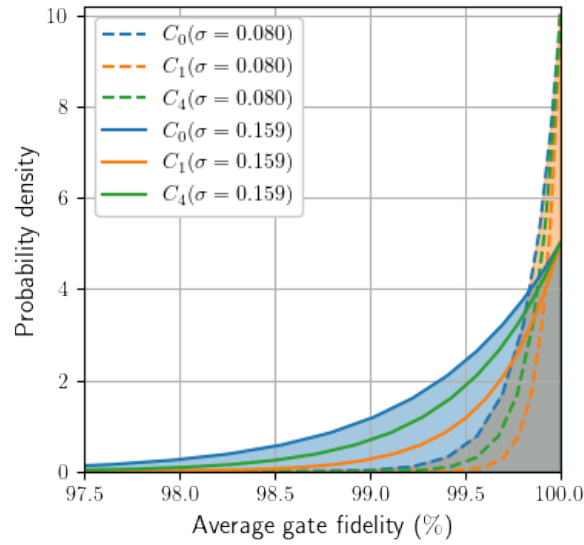
Figure 5.4: **Average gate fidelity distribution of single Clifford gate with stochastic noise in single-qubit model.** Here, we choose C_0, C_1, C_4 in Table 4.1 with $\sigma = 0.080$ and $\sigma = 0.159$ for demonstration. Each of the Clifford gates in this figure has distinct average gate fidelities corresponding to the bars in Fig. 5.3 (a).

unwanted rotating angles to the quantum states in a RB sequence than the slower noise.

5.2.2 Sequence-quasi-static Dephasing Noise

In this section we discussed the RB simulation results with sequence-quasi-static stochastic noise, $T_\sigma = T_{\text{seq}}$. The standard fitting formula with single exponential decay cannot fit this kind of slow-changing noise (See Fig. 5.5). Instead, we use the discrete version of Eq. (3.29) and neglect the perturbation term,

$$P(m) = A \sum_{j=0}^{n} f(\delta_j, \sigma) p_{\delta_j}^m \cdot \Delta + B. \tag{5.6}$$

Here, $n = 100$, σ_{max} is the largest σ we used in the simulations and

$$n\Delta = 6\sigma_{\text{max}},$$

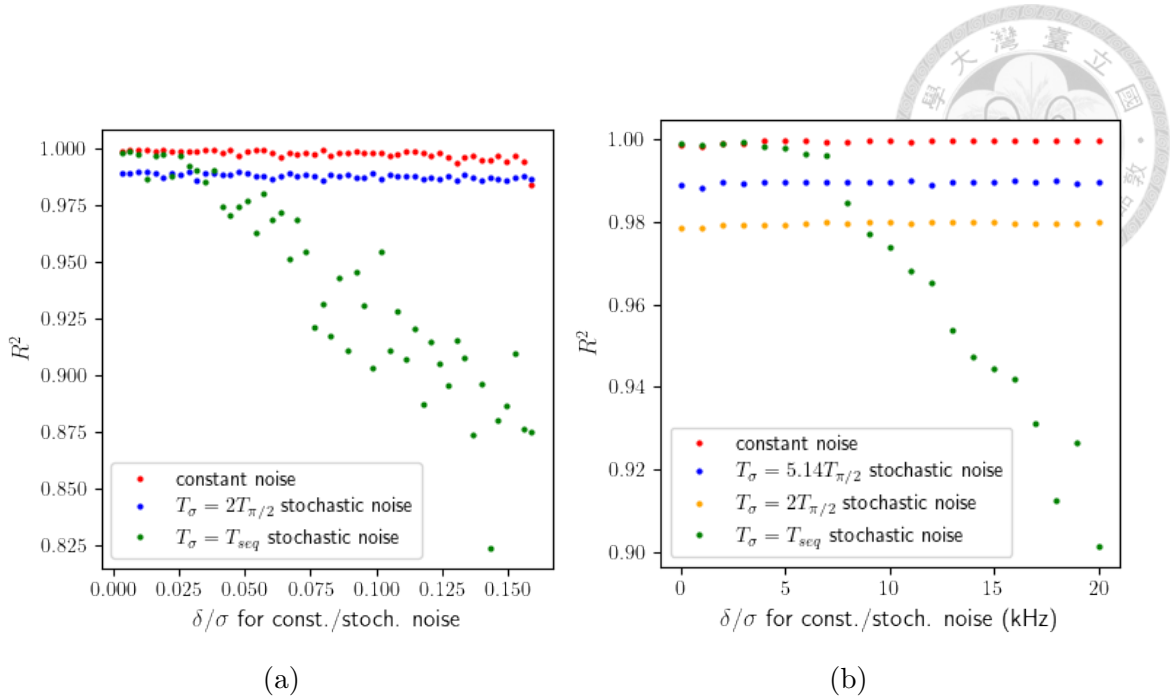$$\delta_j = -3\sigma_{\text{max}} + \frac{6\sigma_{\text{max}} j}{n}.$$

Figure 5.5: R^2 **of different types of noises fitting with** $P(m) = Ap^m + B$**.** Here, we use R^2 as the statistical measure to indicate how well the fitting formula fits the data. B is fixed to $1/2^n$ since there is no SPAM errors in our simulations. For clarity, the blue dots in **(a)** single-qubit results is shifted -0.1, and the blue dots and yellow dots in **(b)** two-qubit results are shifted -0.1 and -0.2 respectively.
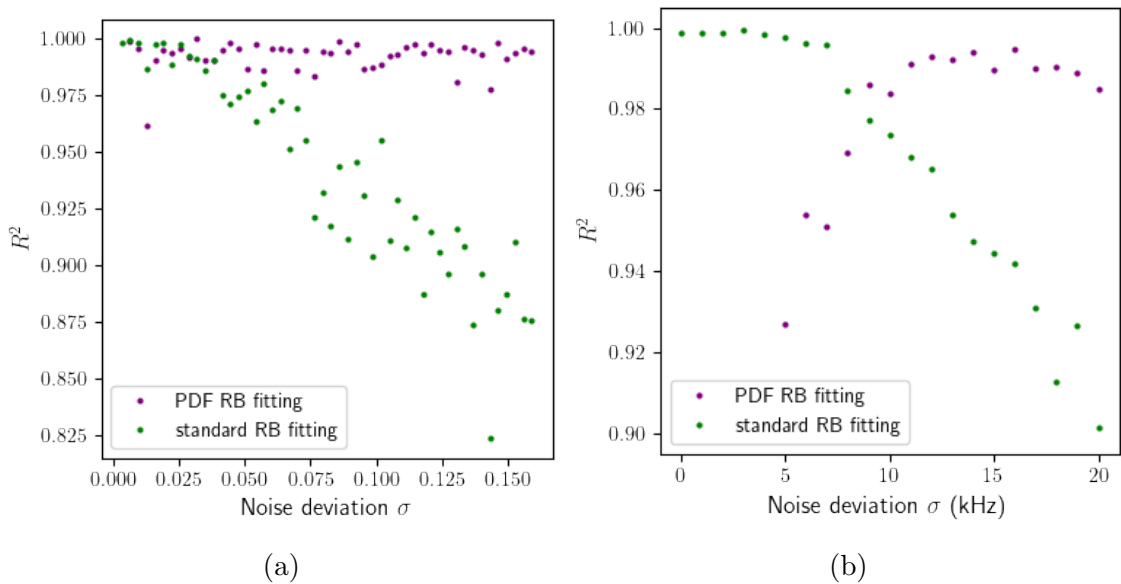

Figure 5.6: R^2 **of sequence-quasi-static noise RB fitting with different for-mulae.** Here, the green dots are R^2 for $P(m) = Ap^m + 1/2^n$ fitting and the purple dots are for PDF RB fitting described in Eq. (5.6) with **(a)** single-qubit results and **(b)** two-qubit results.
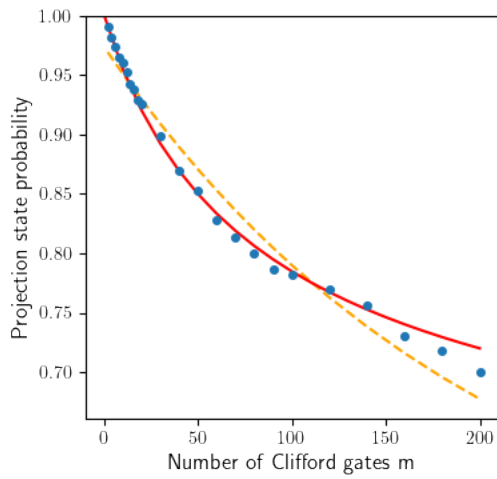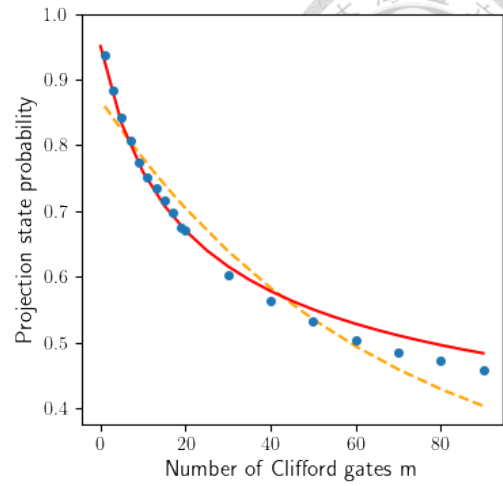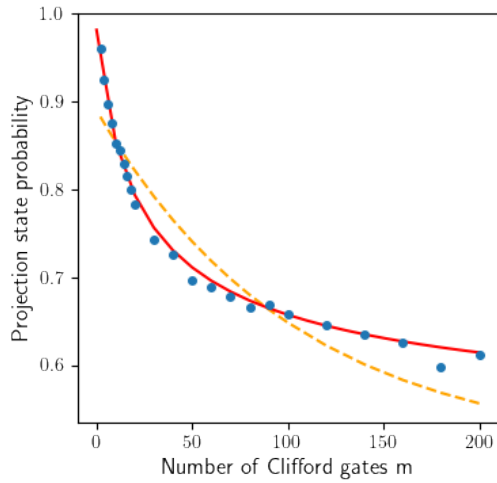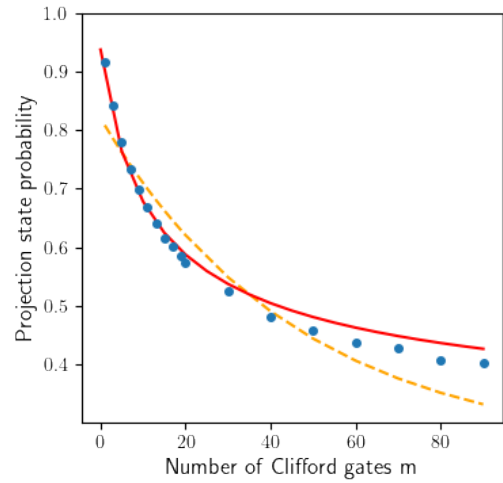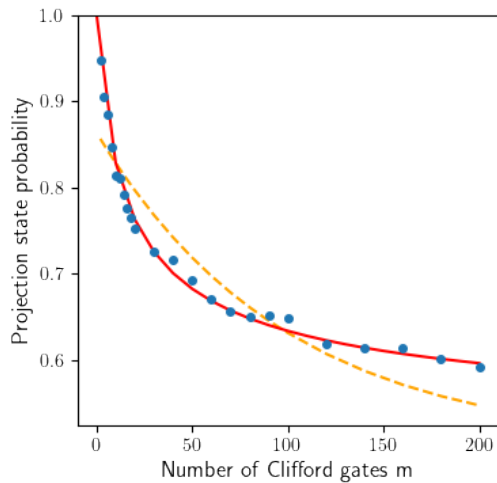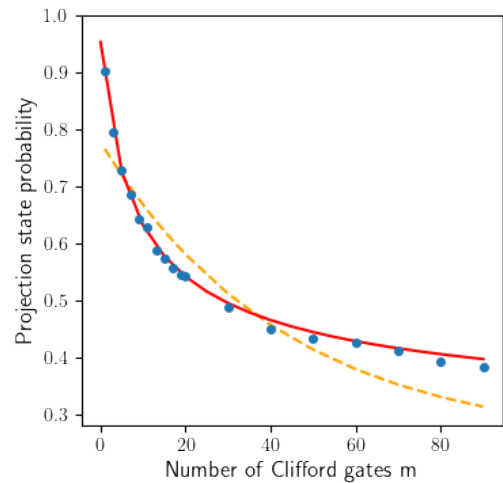
Figure 5.7: **PDF RB fitting with sequence-quasi-static stochastic noise.**
Single-qubit simulations with **(a)** $\sigma = 0.064$, **(b)** $\sigma = 0.127$ and **(c)** $\sigma = 0.159$.
Two-qubit simulations with **(d)** $\sigma = 15\,\text{kHz}$, **(e)** $\sigma = 20\,\text{kHz}$ and **(f)** $\sigma = 25\,\text{kHz}$.
Red curves are the fitting results using Eq. (5.6) and yellow dashed curves are the
fitting results using $P(m) = Ap^m + 1/2^n$.

Hence δ_j is ranged from $-3\sigma_{\max}$ to $3\sigma_{\max}$. We take $\sigma_{\max} = 0.159$ for single-qubit model and $\sigma_{\max} = 20$ kHz for two-qubit model. The range of δ_j ensures the summation in Eq. (5.6) includes at least 99.7% of the probability density described by $f(\delta_j, \sigma)$. It turns out that, due to the imperfect crosstalk error compensation and the limitation of our simulation method, Eq. (5.6) fits the non-exponential decay behaviour of sequence-quasi-static stochastic noise very well (See Fig. 5.6 and 5.7) except for two-qubit simulations under small noise. We calculate conditional $\pi/2$-pulses with time resolution $dt = 5$ ns, which gives a reasonable and controllable simulation time. While dt is not small enough to get perfect conditional $\pi/2$-pulses after crosstalk error compensation as shown in Appendix D. The imperfect crosstalk errors compensation and the time resolution errors dominant for small dephasing noise. Thus the fidelities obtained from two-qubit simulations are a bit lower than theoretical predictions calculated from small dephasing noise. This can be clearly seen in all of our two-qubit simulation results [See the blue dots in Fig. 5.2 (d) and 5.3 (d)].

5.3 Connection with Real Experiment

In this section, we show the connection between our two-qubit simulations and the results described in Ref. [1]. Consider a more general Hamiltonian energy fluctuation noise on all four levels (See Supplementary Information of Ref. [1]),

$$\tilde{H} = \frac{1}{2} \begin{pmatrix} 0 & \gamma_{2\uparrow} B_1 & \gamma_{1\uparrow} B_1 & 0 \\ \gamma_{2\uparrow} B_1^* & \delta\tilde{E}_Z - J & 0 & \gamma_{1\downarrow} B_1 \\ \gamma_{1\uparrow} B_1^* & 0 & -\delta\tilde{E}_Z - J & \gamma_{2\downarrow} B_1 \\ 0 & \gamma_{1\downarrow} B_1^* & \gamma_{2\downarrow} B_1^* & 0 \end{pmatrix} + \begin{pmatrix} \delta_{\uparrow\uparrow} & 0 & 0 & 0 \\ 0 & \delta_{\tilde{\uparrow}\downarrow} & 0 & 0 \\ 0 & 0 & \delta_{\tilde{\downarrow}\uparrow} & 0 \\ 0 & 0 & 0 & \delta_{\downarrow\downarrow} \end{pmatrix}. \quad (5.7)$$

Here, we set the noise being sequence-quasi-static with the same standard deviation for the fluctuations of all four levels, $\sigma = \sigma_{\uparrow\uparrow} = \sigma_{\tilde{\uparrow}\downarrow} = \sigma_{\tilde{\downarrow}\uparrow} = \sigma_{\downarrow\downarrow}$. The simulation shows that the single decay formula cannot fit the RB results properly for the energy
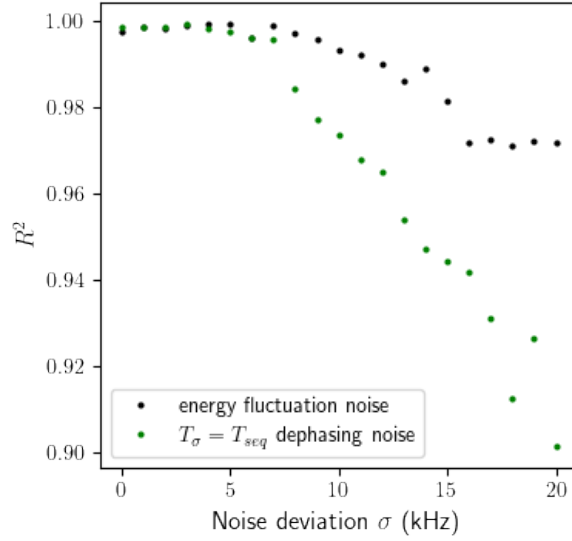
Figure 5.8: R^2 **of energy fluctuation noise fitting with** $P(m) = Ap^m + 0.25$. Hamiltonian fluctuation noise with deviation σ is defined in Eq. (5.7). Here we plot the fitting result for Hamiltonian dephasing noise for comparison.

fluctuation noise, which implies that the non-exponential decay behavior also occurs with more general slow-changing noise (See the black dots in Fig. 5.8). This type of sequence-quasi-static noise simulates the performance of the noise with dominant low-frequency intensities in the noise spectrum, which can be widely seen in silicon-based quantum-dot quantum computing experiments [16–20]. Besides, we can tune the deviation σ of sequence-quasi-static dephasing noise to approximate the real RB experiment in Ref. [1]. We find that $\sigma = 25\,\text{kHz}$ can best simulate the RB experiment (See Fig. 5.9). And we get Clifford fidelity $F_{\text{Clifford}} = 94.69\,\%$ from the fitting function $P(m) = Ap^m + B$, which is almost the same as $F_{\text{Clifford}} = 94.7 \pm 0.8\,\%$ given from the real experiment. Note that, both of these Clifford fidelities are obtained from the single decay formula $P(m) = Ap^m + B$ without fixing A and B. We find out that fitting with unfixed A and B will make the fitting significantly better. It seems that the original single decay fitting formula can fit the RB results with slow-changing noise. While for our two-qubit simulations with sequence-quasi-static noise, the fidelity obtained with unfixed A and B is unreliable. Because B is fitted to be 0.41, which is far from 0.25. The fact that $P(m)$ will not decay to the maximally mixed state probability conflicts with the assumption that there is
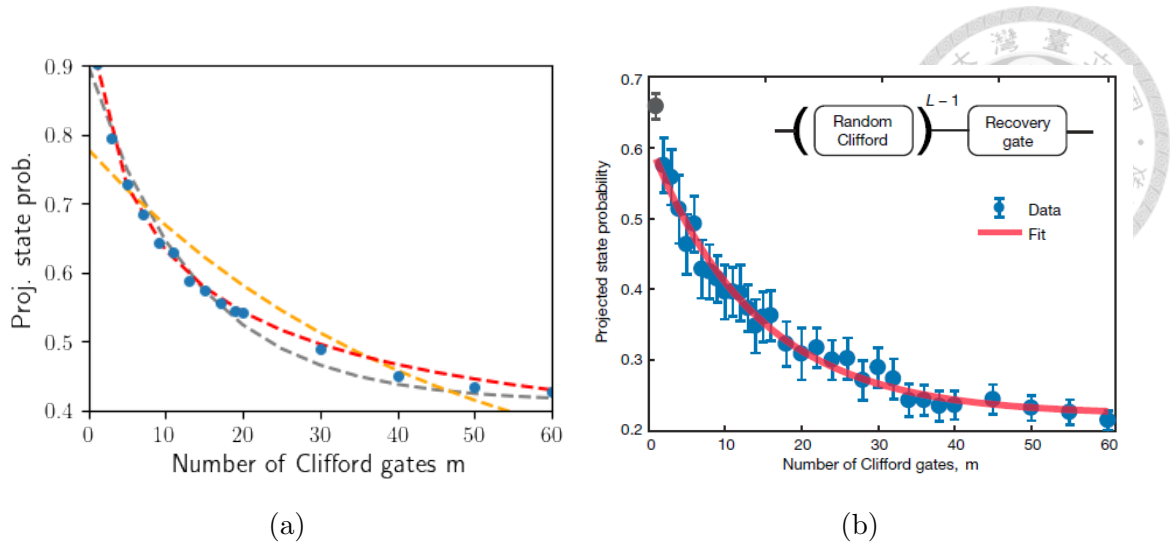
Figure 5.9: **RB simulation compared with the real experiment. (a)** Two-qubit RB simulation with sequence-quasi-static stochastic noise $\sigma = 25$ kHz. Here, the data is fitted by $P(m) = Ap^m + B$ (grey dashed curve), $P(m) = Ap^m + 0.25$ (yellow dashed curve), and PDF RB fitting formula (red dashed curve). **(b)** RB experiment results with real two-qubit silicon-dot device given in Ref. [1].

no SPAM error in the system. In conclusion, the parameters A and B in the single decay formula are supposed to characterize the effect of SPAM errors. If the error is dominated by slow-changing noise, A and B can be misused to fit the effects of slow-changing noise. Then we will obtain the incorrect Clifford fidelity from the RB procedure. We believe that this misfitting problem can be improved by adjusting the RB protocol to eliminate the parameter B [21, 22].

The PDF RB fitting function is significantly better for the non-exponential decay behavior resulted from the slow-changing noise [See the red dashed curve in Fig. 5.9 (a)]. Besides, PDF RB provides clear physical interpretation for the fitting result.

Chapter 6

Conclusions

In this thesis, we have reviewed the RB analysis for constant noise and gate-dependent constant noise. Based on these existing researches, we generalize the analysis to the cases of stochastic noise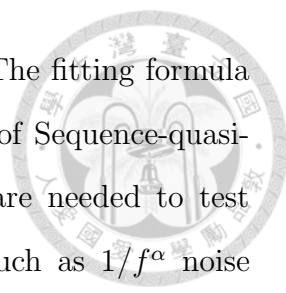. After that, we use a naive simple one-qubit model and a two-qubit model regarding the real experiment to verify the RB theories for different types of noise.

For gate-dependent constant noise, our simulation results show that the analyses in Ref. [11] predict the RB outcomes correctly. Besides, gate-dependent constant RB cannot properly measure the average of the Clifford gates' average gate fidelities. Both our single-qubit and two-qubit models underestimate the proper Clifford fidelity. While further theoretical validation is needed to confirm whether the underestimation is a coincidence or gate-dependent constant RB always underrates the proper Clifford fidelity.

The generalization of Wallman's RB analyses for gate-dependent stochastic noise predicts the RB simulation results well. We find that gate-dependent stochastic noise RB can measure the proper Clifford fidelity. Generally speaking, constant noise is usually identified as systematic noise and is easier to remove. While the randomness of the stochastic noise makes it harder to be perfectly eliminated. Hence our findings about the gate-dependent stochastic noise RB may be good news for real RB experiments.

We proposed a probability density function RB fitting formula to deal with

the noise dominated by slow-changing or low-frequency terms. The fitting formula can appropriately describe the non-exponential decay behavior of Sequence-quasi-static stochastic noise. Further simulations and experiments are needed to test out that whether PDF RB can fit the noise in real devices such as $1/f^\alpha$ noise spectrum. Compared to other non-exponential decay formulae [22–24], PDF RB is more complicated to execute. While we have shown that it is doable for two-qubit devices. The main challenges for carrying out PDF RB are constructing $16^n \times 16^n$ matrices and solving the eigenvalue problems of these matrices. We believe that these are not big problems for several-qubit devices with the help of classical parallel computing. For larger systems such as the leading processors in the noisy intermediate-scale quantum (NISQ) era, which contain fifty to a few hundred qubits, RB protocol is originally not suitable thus these systems are out of our consideration. The main advantages of PDF RB are that it provides clear physical interpretations for the fitting results and is adjustable for different noise distributions.

Appendix A

Explanation of Lemma 1

This appendix gives a brief explanation of Lemma 1 and is based mainly on [33] and [34], but with some of the additional details filled in.

First we introduce the superoperator representation of channels. Consider an $m \times m$ n-qubit density matrix with $m = 2^n$,

$$\rho = \begin{pmatrix} \rho_{11} & \rho_{12} & \cdots & \rho_{1m} \\ \rho_{21} & \rho_{22} & \cdots & \rho_{2m} \\ \vdots & & \ddots & \vdots \\ \rho_{m1} & \rho_{m2} & \cdots & \rho_{mm} \end{pmatrix}. \tag{A.1}$$

Define the vectorization of ρ be column stacking,

$$|\rho\rangle\rangle := \text{vec}(\rho) = (\rho_{11}, \rho_{21}, \ldots, \rho_{m1}, \rho_{12}, \ldots, \rho_{mm})^T. \tag{A.2}$$

For matrices A, B and C, the vectorization map satisfies the identity

$$\text{vec}(ABC) = (C^T \otimes A)\text{vec}(B). \tag{A.3}$$

Consider a CPTP noise channel Λ being expressed in the form

$$\Lambda(\rho) = \sum_i A_i \rho A_i^\dagger. \tag{A.4}$$

The superoperator representation of Λ is defined as

$$\hat{\Lambda} = \sum_i (A_i^* \otimes A_i).$$ (A.5)

By Eq. (A.3) we get

$$|\Lambda(\rho)\rangle\rangle = \hat{\Lambda}|\rho\rangle\rangle.$$ (A.6)

Thus the superoperator representation transforms channel operations acting on ρ into matrix multiplications acting on $|\rho\rangle\rangle$. For example, the superoperator representation of a unitary channel $\mathcal{U}(\rho) = U\rho U^\dagger$ is $\hat{\mathcal{U}} = U^* \otimes U$.

The average gate fidelity of Λ is in the form [33]

$$F_{\text{ave}}(\Lambda, \mathcal{I}) = \frac{\sum_i |\operatorname{Tr}(A_i)|^2 + 2^n}{2^n(2^n + 1)}.$$ (A.7)

Now consider the superoperator of the Haar-twirling on Λ,

$$\hat{\mathcal{W}}_H(\Lambda) = \int_{\mathbf{U}(2^n)} d\eta(U)\, \hat{\mathcal{U}}^\dagger \hat{\Lambda} \hat{\mathcal{U}}.$$ (A.8)

Haar-twirling is unitarily invariant in the sense that

$$\hat{\mathcal{W}}_H(\Lambda) = \hat{\mathcal{V}}^\dagger \hat{\mathcal{W}}_H(\Lambda)\hat{\mathcal{V}}$$ (A.9)

for any $V \in \mathbf{U}(2^n)$. Schur's lemma implies that a unitarily invariant trace-preserving map can only possibly be the form as

$$\mathcal{W}_H(\Lambda)(\rho) = p\rho + (1-p)\operatorname{Tr}(\rho)\frac{I_n}{2^n}.$$ (A.10)

To determine the value of p, note that for any orthonormal basis $|0\rangle, |1\rangle, \ldots, |2^n - 1\rangle$,

$\mathrm{Tr}(\rho) = \sum_i \langle i | \rho | i \rangle$ and $I_n = \sum_i |i\rangle \langle i|$. So

$$\mathcal{W}_H(\Lambda)(\rho) = p\rho + (1-p)\,\mathrm{Tr}(\rho)\frac{I_n}{2^n}$$

$$= pI_n\rho I_n + \frac{(1-p)}{2^n} \sum_i \langle i | \rho | i \rangle \sum_j |j\rangle \langle j| \qquad \text{(A.11)}$$

$$= pI_n\rho I_n + \frac{(1-p)}{2^n} \sum_{i,j} |j\rangle \langle i | \rho | i \rangle \langle j|.$$

Hence the superoperator of $\mathcal{W}_H(\Lambda)(\rho)$ is

$$\hat{\mathcal{W}}_H(\Lambda) = p(I_n \otimes I_n) + \frac{(1-p)}{2^n} \sum_{i,j} |jj\rangle \langle ii|. \qquad \text{(A.12)}$$

Take the trace on the both sides of Eq. (A.12) gives the value of p,

$$p = \frac{\mathrm{Tr}\left(\hat{\mathcal{W}}_H(\Lambda)\right) - 1}{2^{2n} - 1} = \frac{\mathrm{Tr}\,\hat{\Lambda} - 1}{2^{2n} - 1} = \frac{\sum_i |\mathrm{Tr}(A_i)|^2 - 1}{2^{2n} - 1}, \qquad \text{(A.13)}$$

where we have used the fact that $\mathrm{Tr}\,\hat{\Lambda} = \mathrm{Tr}\left(\hat{\mathcal{W}}_H(\Lambda)\right) = \sum_i |\mathrm{Tr}(A_i)|^2$. Substitute Eq. (A.13) into Eq. (A.7) leads to Lemma 1. That is

$$F_{\mathrm{ave}}(\Lambda, \mathcal{I}) = F_{\mathrm{ave}}(\mathcal{W}_H, \mathcal{I}) = p + \frac{1-p}{2^n}. \qquad \text{(A.14)}$$

Appendix B

Wallman's Gate-dependent RB Theory

This appendix gives a brief explanation of the randomized benchmarking theory we mentioned in Sec. 3.1.2, which is proved by Wallman and is based mainly on [11]. Note that the quantum channels we discussed in this thesis are all CPTP maps. While in Wallman's theory, he considers the quantum maps being CP but not necessarily TP. Since the goal of this appendix is to explain the theory in Sec. 3.1.2, here we still focus on the CPTP maps.

B.1   Find the Decay Parameter p

In this section, we discussed how to find the decay parameter for the gate-dependent noise RB. By Theorem 2 in Ref. [11], there exists linear maps $\mathcal{L}$ and $\mathcal{R}$ such that

$$\mathbb{E}_{G_i \in \mathbf{C}_n}(\tilde{\mathcal{G}}_i \circ \mathcal{L} \circ \mathcal{G}_i^\dagger) = \mathcal{L}\mathcal{D}_p \tag{B.1a}$$

$$\mathbb{E}_{G_i \in \mathbf{C}_n}(\mathcal{G}_i^\dagger \circ \mathcal{R} \circ \tilde{\mathcal{G}}_i) = \mathcal{D}_p\mathcal{R}. \tag{B.1b}$$

$$\mathbb{E}_{G_i \in \mathbf{C}_n}(\mathcal{G}_i \circ \mathcal{R}\mathcal{L} \circ \mathcal{G}_i^\dagger) = \mathcal{D}_p. \tag{B.1c}$$

Equation (3.13) is the special case of Eq. (B.1b) with $\tilde{\mathcal{G}}_i = \mathcal{L}_i \circ \mathcal{G}_i \circ \mathcal{R}$ and invertible $\mathcal{R}$. Note that $\mathcal{R}$ is always invertible for Hamiltonian induced unitary noise. Take the unital components of the pauli transfer matrix representations on both sides of Eq. (B.1a) and Eq. (B.1b), that is

$$
\begin{aligned}
\mathbb{E}_{G_i \in \mathbf{C}_n}([\tilde{\mathcal{G}}_i \circ \mathcal{L}' \circ \mathcal{G}_i^{\dagger'}]_{\text{PTM}}) &= p[\mathcal{L}']_{\text{PTM}} \\
\mathbb{E}_{G_i \in \mathbf{C}_n}([\mathcal{G}_i^{\dagger'} \circ \mathcal{R}' \circ \tilde{\mathcal{G}}_i]_{\text{PTM}}) &= p[\mathcal{R}']_{\text{PTM}}.
\end{aligned}
\tag{B.2}
$$

The definition of the unital component of a channel is defined in Eq. (3.16). See the proof of Theorem 2 in Ref. [11] for the calculation details. Equation (B.2) are essentially a pair of eigenvalue equations. Now use the vectorization map described in Eq. (A.3) on the both sides of Eq. (B.2) to obtain the eigenvalue problems that can be solved for p. That is

$$
\begin{aligned}
\mathbb{E}_{G_i \in \mathbf{C}_n}([\mathcal{G}_i']_{\text{PTM}} \otimes [\tilde{\mathcal{G}}_i]_{\text{PTM}}) \text{vec}(\mathcal{L}') &= p\, \text{vec}(\mathcal{L}') \\
\mathbb{E}_{G_i \in \mathbf{C}_n}([\tilde{\mathcal{G}}_i]_{\text{PTM}} \otimes [\mathcal{G}_i']_{\text{PTM}})^T \text{vec}(\mathcal{R}') &= p\, \text{vec}(\mathcal{R}'),
\end{aligned}
\tag{B.3}
$$

where we have used the fact that $[\mathcal{G}]_{\text{PTM}}^T = [\mathcal{G}^\dagger]_{\text{PTM}}$ since the matrix basis is Hermitian.

B.2 Gate-dependent Fitting Formula Derivation

This section gives the derivation of Eq. (3.14). In this section we omit the product symbol $\circ$ of channel composition for simplicity.

First rewrite the expectation average of the RB sequences with length m given in Eq. (3.12) as

$$
\begin{aligned}
\mathcal{S}_m &= \mathbb{E}_{\overrightarrow{G_i} \in (\mathbf{C}_n)^m}(\tilde{\mathcal{G}}_{i_{m+1}:i_1}) = \mathbb{E}_{\overrightarrow{G_i} \in (\mathbf{C}_n)^m}(\tilde{\mathcal{G}}_{i_{m+1}:i_2} \mathcal{L}_{i_1} \mathcal{G}_{i_1} \mathcal{R}) \\
&= \mathbb{E}_{\overrightarrow{G_i} \in (\mathbf{C}_n)^m}(\tilde{\mathcal{G}}_{i_{m+1}:i_2} \mathcal{L} \mathcal{G}_{i_1} \mathcal{R}) + \mathbb{E}_{\overrightarrow{G_i} \in (\mathbf{C}_n)^m}(\tilde{\mathcal{G}}_{i_{m+1}:i_2} \Delta_{i_1}) \\
&= \mathbb{E}_{\overrightarrow{G_i} \in (\mathbf{C}_n)^m}(\tilde{\mathcal{G}}_{i_{m+1}:i_2} \mathcal{L} \mathcal{G}_{i_1} \mathcal{R}) + \mathbb{E}_{\overrightarrow{G_i} \in (\mathbf{C}_n)^m}(\tilde{\mathcal{G}}_{i_{m+1}:i_3} \mathcal{L} \mathcal{G}_{i_2} \mathcal{R} \Delta_{i_1}) \\
&\quad + \mathbb{E}_{\overrightarrow{G_i} \in (\mathbf{C}_n)^m}(\tilde{\mathcal{G}}_{i_{m+1}:i_3} \Delta_{i_2:i_1})
\end{aligned}
\tag{B.4}
$$

where

$$\tilde{\mathcal{G}}_{i_b:i_a} = \bigcirc_{s=a}^{b}\tilde{\mathcal{G}}_{i_s},$$

$$\Delta_{i_b:i_a} = \bigcirc_{s=a}^{b}\Delta_{i_s}, \tag{B.5}$$

$$\Delta_{i_s} = \mathcal{L}_{i_s}\mathcal{G}_{i_s}\mathcal{R} - \mathcal{L}\mathcal{G}_{i_s}\mathcal{R}$$

and $\mathcal{L}$ is defined in Eq. (B.1a). The first term on the right hand side of Eq. (B.4) gives

$$\mathbb{E}_{\overrightarrow{G_i}\in(\mathbf{C}_n)^m}(\tilde{\mathcal{G}}_{i_{m+1}:i_2}\mathcal{L}\mathcal{G}_{i_1}\mathcal{R}) = \mathbb{E}_{\overrightarrow{G_i}\in(\mathbf{C}_n)^m}[\tilde{\mathcal{G}}_{i_{m+1}:i_2}\mathcal{L}(\mathcal{G}_{i_{m+1}:i_2}^{\dagger})\mathcal{R}]$$
$$= \mathcal{L}\mathcal{D}_p^m\mathcal{R}, \tag{B.6}$$

where we have used Eq. (B.1a) m times and the fact that $\mathcal{G}_{i_{m+1}:i_1} = \mathcal{I}$. Now consider

$$\mathbb{E}_{\overrightarrow{G_i}\in(\mathbf{C}_n)^m}(\tilde{\mathcal{G}}_{i_{m+1}:i_{j+1}}\mathcal{L}\mathcal{G}_{i_j}\mathcal{R}\Delta_{i_{j-1}:i_1})$$
$$= \mathbb{E}_{\overrightarrow{G_i}\in(\mathbf{C}_n)^m}[\tilde{\mathcal{G}}_{i_{m+1}:i_{j+1}}\mathcal{L}(\mathcal{G}_{i_{m+1}:i_{j+1}}^{\dagger})(\mathcal{G}_{i_{j-1}:i_1}^{\dagger})\mathcal{R}\Delta_{i_{j-1}:i_1}]$$
$$= \mathbb{E}_{\overrightarrow{G_i}\in(\mathbf{C}_n)^m}[\tilde{\mathcal{G}}_{i_{m+1}:i_{j+1}}\mathcal{L}(\mathcal{G}_{i_{m+1}:i_{j+1}}^{\dagger})(\mathcal{G}_{i_{j-2}:i_1}^{\dagger})\mathcal{G}_{i_{j-1}}^{\dagger}\mathcal{R}\Delta_{i_{j-1}}\Delta_{i_{j-2}:i_1}]$$
$$= \mathbb{E}_{\overrightarrow{G_i}\in(\mathbf{C}_n)^m}[\tilde{\mathcal{G}}_{i_{m+1}:i_{j+1}}\mathcal{L}(\mathcal{G}_{i_{m+1}:i_{j+1}}^{\dagger})(\mathcal{G}_{i_{j-2}:i_1}^{\dagger})(\mathcal{G}_{i_{j-1}}^{\dagger}\mathcal{R}\tilde{\mathcal{G}}_{i_{j-1}})\Delta_{i_{j-2}:i_1}] \tag{B.7}$$
$$- \mathbb{E}_{\overrightarrow{G_i}\in(\mathbf{C}_n)^m}[\tilde{\mathcal{G}}_{i_{m+1}:i_{j+1}}\mathcal{L}(\mathcal{G}_{i_{m+1}:i_{j+1}}^{\dagger})(\mathcal{G}_{i_{j-2}:i_1}^{\dagger})(\mathcal{G}_{i_{j-1}}^{\dagger}\mathcal{R}\mathcal{L}\mathcal{G}_{i_{j-1}})\mathcal{R}\Delta_{i_{j-2}:i_1}]$$
$$= 0.$$

The last equality is from Eq. (B.1b) and Eq.(B.1c),

$$\mathcal{G}_{i_{j-1}}^{\dagger}\mathcal{R}\tilde{\mathcal{G}}_{i_{j-1}} = \mathcal{D}_p\mathcal{R}$$
$$\mathcal{G}_{i_{j-1}}^{\dagger}\mathcal{R}\mathcal{L}\mathcal{G}_{i_{j-1}} = \mathcal{D}_p. \tag{B.8}$$

Thus the second term on the right hand side of Eq. (B.4) vanishes. Besides, we can recursively decompose the third term into

$$\mathbb{E}_{\overrightarrow{G_i}\in(\mathbf{C}_n)^m}(\tilde{\mathcal{G}}_{i_{m+1}:i_j}\Delta_{i_{j-1}:i_1}) = \mathbb{E}_{\overrightarrow{G_i}\in(\mathbf{C}_n)^m}(\tilde{\mathcal{G}}_{i_{m+1}:i_{j+1}}\mathcal{L}\mathcal{G}_{i_j}\mathcal{R}\Delta_{i_{j-1}:i_1})$$
$$+ \mathbb{E}_{\overrightarrow{G_i}\in(\mathbf{C}_n)^m}(\tilde{\mathcal{G}}_{i_{m+1}:i_{j+1}}\Delta_{i_j:i_1}), \tag{B.9}$$

where the first terms always vanish. Finally Eq. (B.4) becomes

$$\mathcal{S}_m = \mathcal{L}\mathcal{D}_p^m\mathcal{R} + \mathbb{E}_{\overrightarrow{G_i}\in(\mathbf{C}_n)^m}(\Delta_{i_{m+1}:i_1}). \tag{B.10}$$

48

The projection state probability of $\mathcal{S}_m$ is

$$
\begin{aligned}
P(m) &= \mathrm{Tr}[\mathcal{S}_m(\rho_\psi)E_\psi] \\
&= \mathrm{Tr}\big[\mathcal{L}\mathcal{D}_p^m\mathcal{R}(\rho_\psi)E_\psi\big] + \mathrm{Tr}\Big[\mathbb{E}_{\overrightarrow{G_i}\in(\mathbf{C}_n)^m}(\Delta_{i_{m+1}:i_1})(\rho_\psi)E_\psi\Big] \\
&= \mathrm{Tr}\Big[\mathcal{L}\left(p^m\mathcal{R}(\rho_\psi) + \frac{1-p^m}{2^n}I_n\right)E_\psi\Big] + \mathrm{Tr}\Big[\mathbb{E}_{\overrightarrow{G_i}\in(\mathbf{C}_n)^m}(\Delta_{i_{m+1}:i_1})(\rho_\psi)E_\psi\Big] \\
&= \mathrm{Tr}[\mathcal{L}\mathcal{R}(\rho_\psi)E_\psi]p^m + \mathrm{Tr}\Big[\mathcal{L}\left(\frac{I_n}{2^n}\right)E_\psi\Big](1-p^m) + \mathrm{Tr}\Big[\mathbb{E}_{\overrightarrow{G_i}\in(\mathbf{C}_n)^m}(\Delta_{i_{m+1}:i_1})(\rho_\psi)E_\psi\Big] \\
&= Ap^m + B + \epsilon_m,
\end{aligned}
\tag{B.11}
$$

where

$$
\begin{aligned}
A &:= \mathrm{Tr}\Big[\mathcal{L}\left(\mathcal{R}(\rho_\psi) - \frac{I_n}{2^n}\right)E_\psi\Big] \\
B &:= \mathrm{Tr}\Big[\mathcal{L}\left(\frac{I_n}{2^n}\right)E_\psi\Big] \\
\epsilon_m &:= \mathrm{Tr}\Big[\mathbb{E}_{\overrightarrow{G_i}\in(\mathbf{C}_n)^m}(\Delta_{i_{m+1}:i_1})(\rho_\psi)E_\psi\Big].
\end{aligned}
\tag{B.12}
$$

Hence Eq. (3.14) is proved.

Appendix C

Rotating Frame Transformation

In Sec. 4.2.1 we use a time-dependent rotating frame to observe the action of the Hamiltonian with oscillating magnetic field B_1 operating on the resonance frequency. Begin with the Schrödinger equation for the time-evolution operator $U(t) |\psi(0)\rangle = |\psi(t)\rangle$,

$$\dot{U}(t) = -\frac{iH}{\hbar} U(t). \tag{C.1}$$

Insert a unitary transformation $R(t)$ on both sides and use the fact that $R^\dagger R = I$, we get

$$R\dot{U} = -\frac{i}{\hbar}(RHR^\dagger)RU. \tag{C.2}$$

The product rule of derivative gives

$$R\dot{U} = \frac{d}{dt}(RU) - \dot{R}U = \frac{d}{dt}(RU) - \dot{R}R^\dagger RU. \tag{C.3}$$

Substitute Eq. (C.3) into Eq. (C.2) to obtain the Schrödinger equation after transformation:

$$\frac{d}{dt}(RU) = -\frac{i}{\hbar}(RHR^\dagger + i\dot{R}R^\dagger)RU. \tag{C.4}$$

Define the time-evolution operator after the transformation as $U'(t) = R(t)U(t)$. The effective Hamiltonian for $U'(t)$ is $H' = RHR^\dagger + i\dot{R}R^\dagger$.

As shown in Eq. (4.14), $R(t)$ for the two-qubit rotating frame transformation is diagonal. Thus the measurement result of the final state $|\psi(t)\rangle$ is identical to the

result of the transformed state $R(t) |\psi(t)\rangle$. This is the reason why we can calculate gate-dependent noise channels with the rotating frame Hamiltonian in Sec. 4.2.2 even though the measurements are taken in the original frame.
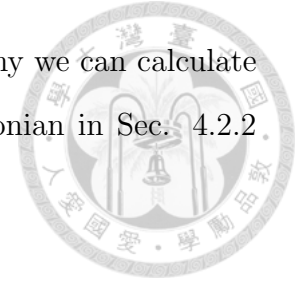
Appendix D

Virtual-phase Gate Implementation

This appendix demonstrates how to generate zero-gate-time arbitrary virtual-phase rotations with the phase offset of ESR drives. The implementing method is based mainly on [35].

First consider virtual-Z implementation in single-qubit devices. Assume the Hamiltonian in the rotating frame is
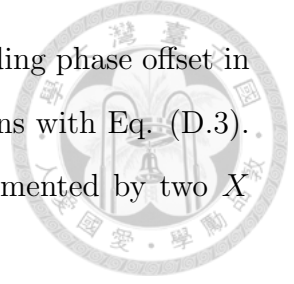
$$H = \frac{1}{2} \begin{pmatrix} 0 & Be^{i\omega t} \\ Be^{-i\omega t} & 0 \end{pmatrix}. \tag{D.1}$$

Here, ω is the resonance frequency and B is the ESR pulse. For the on resonance drive, $B(t) = \Omega e^{-i(\omega t + \phi)}$ with Rabi frequency Ω and phase offset ϕ. Then

$$H = \frac{1}{2} \begin{pmatrix} 0 & \Omega e^{-i\phi} \\ \Omega e^{i\phi} & 0 \end{pmatrix} = \frac{1}{2}\Omega[\cos(\phi)X + \sin(\phi)Y] \tag{D.2}$$

the time evolution of the Hamiltonian gives the unitary gates written as

$$e^{-i\frac{\theta}{2}[\cos(\phi)X+\sin(\phi)Y]} = \cos\left(\frac{\theta}{2}\right)I - i\sin\left(\frac{\theta}{2}\right)[\cos(\phi)X + \sin(\phi)Y]$$
$$= Z_\phi X_\theta Z_{-\phi}. \tag{D.3}$$

52

Thus X rotations are conjugated by virtual-Z rotations after adding phase offset in ESR pulses. We can generate arbitrary zero-gate-time Z rotations with Eq. (D.3). For example, a sequence of operations $X_{\theta_3}Z_{\theta_2}X_{\theta_1}$ can be implemented by two X pulses:

$$e^{-i\frac{\theta_3}{2}[\cos(-\theta_2)X+\sin(-\theta_2)Y]}e^{-i\frac{\theta_1}{2}[\cos(0)X+\sin(0)Y]} = (Z_{-\theta_2}X_{\theta_3}Z_{\theta_2})(X_{\theta_1}). \qquad (D.4)$$

Note that the last gate $Z_{-\theta_2}$ does not affect the measurement results, which are measured along Z.

As shown in Eq. (4.15) and Eq. (4.16), the rotating frame Hamiltonian for generating $\pi/2$-pulses in our two-qubit model are essentially one-qubit Hamiltonian Eq.(D.2) in different axes. Thus we can implement arbitrary two-qubit phase gates using the similar method for one-qubit system. An arbitrary two-qubit phase gate in the rotating frame can be written as

$$P = \begin{pmatrix} e^{i\phi_{\uparrow\uparrow}} & 0 & 0 & 0 \\ 0 & e^{i\phi_{\tilde{\uparrow}\downarrow}} & 0 & 0 \\ 0 & 0 & e^{i\phi_{\downarrow\tilde{\uparrow}}} & 0 \\ 0 & 0 & 0 & e^{i\phi_{\downarrow\downarrow}} \end{pmatrix}. \qquad (D.5)$$

P can be implemented virtually by adding the phase offset corresponding to the relative phase of the resonance states on the future pulses. For example, since $U_{1\uparrow}^{\pm\pi/2}$ operates on the states $(\uparrow\uparrow, \downarrow\tilde{\uparrow})$, the future $U_{1\uparrow}^{\pm\pi/2}$ pulses after the operation P should be implemented with an additional phase offset $\phi_{1\uparrow} = (\phi_{\uparrow\uparrow} - \phi_{\downarrow\tilde{\uparrow}})$ added on the oscillating magnetic field B_1. From Eq. (D.3), this is equivalent to apply a virtual-Z rotation on the states $(\uparrow\uparrow, \downarrow\tilde{\uparrow})$ before $U_{1\uparrow}^{\pm\pi/2}$ pulses:

$$Z_{-\phi_{1\uparrow}} = \begin{pmatrix} e^{i\frac{\phi_{1\uparrow}}{2}} & 0 \\ 0 & e^{-i\frac{\phi_{1\uparrow}}{2}} \end{pmatrix} = e^{-i\frac{(\phi_{\uparrow\uparrow}+\phi_{\downarrow\tilde{\uparrow}})}{2}} \begin{pmatrix} e^{i\phi_{\uparrow\uparrow}} & 0 \\ 0 & e^{i\phi_{\downarrow\tilde{\uparrow}}} \end{pmatrix}, \qquad (D.6)$$

which is exactly the same action as P on the states $(\uparrow\uparrow, \downarrow\tilde{\uparrow})$. In our two-qubit

$\pi/2$-pulse	$F_{\mathbf{uncorrected}}$ (%)	$F_{\mathbf{corrected}}$ (%)
$U_{1\uparrow}^{\pi/2}$	99.481	99.977
$U_{1\downarrow}^{\pi/2}$	99.465	99.965
$U_{2\uparrow}^{\pi/2}$	99.465	99.965
$U_{2\downarrow}^{\pi/2}$	99.481	99.977

Table D.1: **Trace fidelity of $\pi/2$-pulses corrected by virtual-phase implementation**. Here, the two-qubit trace fidelity is defined as $F = |\mathrm{Tr}(\tilde{U}U^\dagger)|^2/16$. The time resolution of every conditional $\pi/2$-pulse is $dt = 5$ ns. The imperfect crosstalk error compensation and the time resolution limit the fidelity after correction.
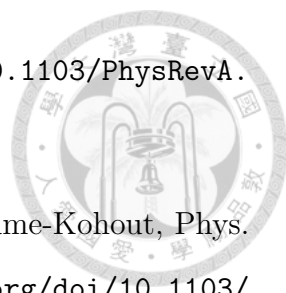
simulations, we use virtual-phase gates to compensate phase errors from the crosstalk terms (See Table D.1) and generate virtual-$Z_{\pi/2}$ gates on Q1 and Q2:
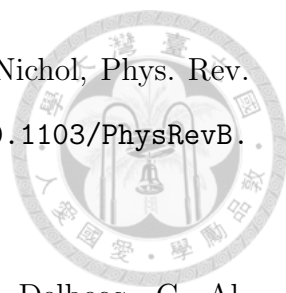
$$
\begin{aligned}
[Z_{\pi/2}]_1 := Z_{\pi/2} \otimes I &= \begin{pmatrix} e^{-i\frac{\pi}{4}} & 0 & 0 & 0 \\ 0 & e^{-i\frac{\pi}{4}} & 0 & 0 \\ 0 & 0 & e^{i\frac{\pi}{4}} & 0 \\ 0 & 0 & 0 & e^{i\frac{\pi}{4}} \end{pmatrix}, \\
[Z_{\pi/2}]_2 := I \otimes Z_{\pi/2} &= \begin{pmatrix} e^{-i\frac{\pi}{4}} & 0 & 0 & 0 \\ 0 & e^{i\frac{\pi}{4}} & 0 & 0 \\ 0 & 0 & e^{-i\frac{\pi}{4}} & 0 \\ 0 & 0 & 0 & e^{i\frac{\pi}{4}} \end{pmatrix}.
\end{aligned} \tag{D.7}
$$

Bibliography

[1] W. Huang, C. H. Yang, K. W. Chan, T. Tanttu, B. Hensen, R. C. C. Leon, M. A. Fogarty, J. C. C. Hwang, F. E. Hudson, K. M. Itoh, et al., Nature **569**, 532 (2019), ISSN 1476-4687, URL https://doi.org/10.1038/s41586-019-1197-0.

[2] X. Xue, T. F. Watson, J. Helsen, D. R. Ward, D. E. Savage, M. G. Lagally, S. N. Coppersmith, M. A. Eriksson, S. Wehner, and L. M. K. Vandersypen, Phys. Rev. X **9**, 021011 (2019), URL https://link.aps.org/doi/10.1103/PhysRevX.9.021011.

[3] P. Shor, in *Proceedings 35th Annual Symposium on Foundations of Computer Science* (1994), pp. 124–134.

[4] L. K. Grover, in *Proceedings of the Twenty-Eighth Annual ACM Symposium on Theory of Computing* (Association for Computing Machinery, New York, NY, USA, 1996), STOC '96, p. 212–219, ISBN 0897917855, URL https://doi.org/10.1145/237814.237866.

[5] E. Magesan, J. M. Gambetta, and J. Emerson, Phys. Rev. A **85**, 042311 (2012), URL https://link.aps.org/doi/10.1103/PhysRevA.85.042311.

[6] J. J. Wallman and S. T. Flammia, New Journal of Physics **16**, 103032 (2014), URL https://doi.org/10.1088/1367-2630/16/10/103032.

[7] J. M. Epstein, A. W. Cross, E. Magesan, and J. M. Gambetta, Phys. Rev.

A **89**, 062321 (2014), URL `https://link.aps.org/doi/10.1103/PhysRevA.89.062321`.

[8] T. Proctor, K. Rudinger, K. Young, M. Sarovar, and R. Blume-Kohout, Phys. Rev. Lett. **119**, 130502 (2017), URL `https://link.aps.org/doi/10.1103/PhysRevLett.119.130502`.

[9] H. Ball, T. M. Stace, S. T. Flammia, and M. J. Biercuk, Phys. Rev. A **93**, 022303 (2016), URL `https://link.aps.org/doi/10.1103/PhysRevA.93.022303`.

[10] J. Qi and H. Ng, International Journal of Quantum Information **17**, 1950031 (2019).

[11] J. J. Wallman, Quantum **2**, 47 (2018), ISSN 2521-327X, URL `https://doi.org/10.22331/q-2018-01-29-47`.

[12] P. Figueroa-Romero, K. Modi, R. J. Harris, T. M. Stace, and M.-H. Hsieh, PRX Quantum **2**, 040351 (2021), URL `https://link.aps.org/doi/10.1103/PRXQuantum.2.040351`.

[13] J. Miguel-Ramiro, A. Pirker, and W. Dür, Phys. Rev. Research **3**, 033038 (2021), URL `https://link.aps.org/doi/10.1103/PhysRevResearch.3.033038`.

[14] J. Wallman, C. Granade, R. Harper, and S. T. Flammia, New Journal of Physics **17**, 113020 (2015), URL `https://doi.org/10.1088/1367-2630/17/11/113020`.

[15] T. Chasseur and F. K. Wilhelm, Phys. Rev. A **92**, 042333 (2015), URL `https://link.aps.org/doi/10.1103/PhysRevA.92.042333`.

[16] A. V. Kuhlmann, J. Houel, A. Ludwig, L. Greuter, D. Reuter, A. D. Wieck, M. Poggio, and R. J. Warburton, Nature Physics **9**, 570 (2013), ISSN 1745-2481, URL `https://doi.org/10.1038/nphys2688`.

[17] E. J. Connors, J. Nelson, H. Qiao, L. F. Edge, and J. M. Nichol, Phys. Rev. B **100**, 165305 (2019), URL https://link.aps.org/doi/10.1103/PhysRevB.100.165305.

[18] J. Yoneda, K. Takeda, T. Otsuka, T. Nakajima, M. R. Delbecq, G. Allison, T. Honda, T. Kodera, S. Oda, Y. Hoshi, et al., Nature Nanotechnology **13**, 102 (2018), ISSN 1748-3395, URL https://doi.org/10.1038/s41565-017-0014-x.

[19] T. Nakajima, A. Noiri, K. Kawasaki, J. Yoneda, P. Stano, S. Amaha, T. Otsuka, K. Takeda, M. R. Delbecq, G. Allison, et al., Phys. Rev. X **10**, 011060 (2020), URL https://link.aps.org/doi/10.1103/PhysRevX.10.011060.

[20] K. W. Chan, W. Huang, C. H. Yang, J. C. C. Hwang, B. Hensen, T. Tanttu, F. E. Hudson, K. M. Itoh, A. Laucht, A. Morello, et al., Phys. Rev. Applied **10**, 044017 (2018), URL https://link.aps.org/doi/10.1103/PhysRevApplied.10.044017.

[21] R. Harper, I. Hincks, C. Ferrie, S. T. Flammia, and J. J. Wallman, Phys. Rev. A **99**, 052350 (2019), URL https://link.aps.org/doi/10.1103/PhysRevA.99.052350.

[22] M. A. Fogarty, M. Veldhorst, R. Harper, C. H. Yang, S. D. Bartlett, S. T. Flammia, and A. S. Dzurak, Phys. Rev. A **92**, 022326 (2015), URL https://link.aps.org/doi/10.1103/PhysRevA.92.022326.

[23] M. Veldhorst, J. C. C. Hwang, C. H. Yang, A. W. Leenstra, B. de Ronde, J. P. Dehollain, J. T. Muhonen, F. E. Hudson, K. M. Itoh, A. Morello, et al., Nature Nanotechnology **9**, 981 (2014), ISSN 1748-3395, URL https://doi.org/10.1038/nnano.2014.216.

[24] J. Qi and H. K. Ng, Phys. Rev. A **103**, 022607 (2021), URL https://link.aps.org/doi/10.1103/PhysRevA.103.022607.

[25] C. J. Wood, J. D. Biamonte, and D. G. Cory (2011), URL `https://arxiv.org/abs/1111.6950`.

[26] C. J. Colbourn and J. H. Dinitz, eds., *Handbook of Combinatorial Designs*, Discrete Mathematics and Its Applications (Chapman & Hall/CRC, Philadelphia, PA, 2006), 2nd ed.

[27] O. D. Matteo (2014), URL `https://glassnotes.github.io/OliviaDiMatteo_Unitary2Designs.pdf`.

[28] C. Dankert, R. Cleve, J. Emerson, and E. Livine, Phys. Rev. A **80**, 012304 (2009), URL `https://link.aps.org/doi/10.1103/PhysRevA.80.012304`.

[29] PennyLane dev team, *Understanding the Haar Measure — PennyLane* (2021), URL `https://pennylane.ai/qml/demos/tutorial_haar_measure.html#id3`.

[30] C. H. Bennett, D. P. DiVincenzo, J. A. Smolin, and W. K. Wootters, Phys. Rev. A **54**, 3824 (1996), URL `https://link.aps.org/doi/10.1103/PhysRevA.54.3824`.

[31] M. A. Nielsen and I. L. Chuang, *Quantum Computation and Quantum Information: 10th Anniversary Edition* (Cambridge University Press, USA, 2011), 10th ed., ISBN 1107002176.

[32] Qiskit Development Team, *qiskit.quantum_info.average_gate_fidelity — Qiskit 0.36.2 documentation*, URL `https://qiskit.org/documentation/stubs/qiskit.quantum_info.average_gate_fidelity.html`.

[33] M. A. Nielsen, Physics Letters A **303**, 249 (2002), ISSN 0375-9601, URL `https://www.sciencedirect.com/science/article/pii/S0375960102012720`.

[34] J. Emerson, R. Alicki, and K. Życzkowski, Journal of Optics B: Quantum and Semiclassical Optics **7**, S347 (2005), URL `https://doi.org/10.1088/1464-4266/7/10/021`.

[35] D. C. McKay, C. J. Wood, S. Sheldon, J. M. Chow, and J. M. Gambetta, Phys. Rev. A **96**, 022330 (2017), URL `https://link.aps.org/doi/10.1103/PhysRevA.96.022330`.